D.T1.5.2 Applying remote sensing techniques to identify and monitor forest disturbances

WP 1 PRONA

Responsibility for Deliverable

Christian Ginzler (WSL)

Contributors

Marc Adams (BFW), Anne Hormes (BFW), Veronika Lechner (BFW)

Innsbruck, December 2019

GreenRisk4Alps Partnership

BFW	Austrian Forest Research Center (AT)
DISAFA	Department of Agricultural, Forest and Food Sciences, University of Turin (ITA)
EURAC	European Academy of Bozen-Bolzano – EURAC Research (ITA)
INRAE	French national research institute for agriculture, food and the environment, Grenoble regional centre (FRA)
LWF	Bavarian State Institute of Forestry (GER)
MFM	Forestry company Franz-Mayr-Melnhof-Saurau (AT)
SFM	Safe Mountain Foundation (ITA)
UL	University of Ljubljana, Biotechnical Faculty, Department of Forestry and Renewable Resources (SLO)
UGOE	University of Göttingen, Department of Forest and Nature Conservation Policy (GER)
WSL	Swiss Federal Institute for Forest, Snow and Landscape Research (CH)
WLV	Austrian Service for Torrent and Avalanche Control (AT)
SFS	Slovenia Forest Service (SLO)

Contents

Abbreviations 4
Figures 5
Tables 7
Introduction 8
Overview of EO-techniques 10
Satellites 10
Unmanned Aerial Systems 11
Case Studies 13
Rapid assessment of Storm Damages with Sentinel-1AB 13
Introduction 13
Study areas and data 15
Results 17
Presentation and dissemination of results 17
Analysis of drought effects after the dry/hot summer 2018 18
Introduction 18
Remote sensing data 19
Mapping drought stress on forests 19
Mapping forest disturbances in 2019 20
Additional datasets 21
Results 24
Drought stress on forests 24
Forest disturbances in 2019 27
Link between drought stress in 2018 and disturbances in 2019 29
Discussion and conclusion 30
Fungal infestation of *Pinus nigra* in Lower Austria with UAS 32
Background 32
UAS campaign 34
Monitoring a forest fire area in Tyrol (UAS) 38

Satellite platforms for forest monitoring and hazard mapping 46
Appendix 54
References 56

Abbreviations

AdTLR	Office of the Tyrolean Regional Government
CIR	Colour Infrared
EO	Earth Observation
InSAR	Interferometric synthetic aperture radar
LiDAR	Light Detection and Ranging
RGB	Red Green Blue
SAR	Synthethic aperture radar
S1/S2	Sentinel 1 / 2
UAS	Unmanned Aerial Systems (aircraft including controlling unit)
WLV	Austrian Service for Torrent and Avalanche Control

Figures

Figure 1: Frequency map for the minimum number of SAR images of Sentinel-1. 14

Figure 2: Localisation of the various storm damage cases processed 15

Figure 3: Representation of the coordinate pairs of indications for storm damage with a minimum area of 0.5 ha. On the left, a general overview of Switzerland after "Burglind", on the right, a greatly enlarged section near Kestenholz (SO). The interactive result for the whole of Switzerland can be accessed at https://tinyurl.com/Hinweis-Cluster. © Open street map. 18

Figure 4: Study area (left) and Sentinel-2 tiles covering Switzerland (right) 19

Figure 5: Example of the forest mask (right) used in this study around the city of Schaffhausen. Areas of forest not covered by the mask (top right, left bottom) are outside the study region. 22

Figure 6: Example of the forest mixture dataset used for this study around the city of Schaffhausen. Darker green colors represent pure needleleaf forest areas, light green needleleaf-dominated, light red deciduous-dominated and dark red pure deciduous forest areas. 23

Figure 7: Spatial distribution (in red) of Picea abies (left) and Fagus sylvatica (right) around the area of Schaffhausen. Notice that since these data represent the potential spatial distribution of the species they are not mutually exclusive. Thus, a significant spatial overlap can be observed. 23

Figure 8: Example of the vegetation height dataset used for this study around the city of Schaffhausen. Green colors indicate trees with a height between 3-15m, blue trees with a height between 15-25m and red color trees higher than 25m. 24

Figure 9: NDWI anomalies for 2018 for the extent of the study region. 25

Figure 10: Percent of total forest area under severe water stress per canton within the study region. The numbers on top of the bars represent the actual forest area in ha (based on the NFI forest mask) under severe water stress. 26

Figure 11: Percent of forest species potentially present at the areas under severe water stress in 2018. 27

Figure 12: Forest disturbances in 2019 for the extent of the study region. 28

Figure 13: Percent of forest disturbances relative to the total forest area per canton within the study region. The numbers on top of the bars represent the actual forest area of disturbances in ha. 29

Figure 14: Relationship between forest areas where disturbances were detected in 2019 and their respective NDWI anomalies in 2018. For clarity, NDWI anomalies of 2018 are reclassified to four classes 30

Figure 15 Black pine stands near Steinfeld showing different degrees of Diplodia sapinea infestation. 33

Figure 16 Multiplex Mentor UAS (left); daylight (Sony NEX5) and multispectral (Mica Sense RedEdge 3) cameras used on-board the Mentor, with corresponding spectral range (sources: MicaSense, dpreview.com, BFW)..... 35

Figure 17 UAS-OP of the study site; overview (left) and detail (right)..... 36

Figure 18 Comparison of RGB (left) and NDVI (right) imagery over infected Pinus nigra crowns (circled in blue). 36

Figure 19 Subplot of Pinus nigra crowns classified into healthy (green), infected (orange) and dead (red) classes. 37

Figure 20 Distribution of NDVI-values within tree classes 1-3 (left) and relative frequency of trees classified as healthy, infected and dead within the same classes..... 37

Figure 21 Overview of lower burnt section at the Hochmahdkopf on 24 April 2014 (left); damaged avalanche defense structures and charred mountain pine in the upper burnt section on 10 April 2014 (right). 39

Figure 22 Results of the data collection on 4 July 2017 - orthophoto (top) in overview (left) and detail (right) (GSD: 0.05 m), Relief of the DSM (bottom) in overview (left) and detail (right) (GSD: 0.2 m); the red polygon indicates the enlarged area. 40

Figure 23 Comparison of the shares of the erosion classes in 2015 and 2017 (left); examples of the erosion classes based on the orthophoto 2017 (I - high, II - medium, III - low) (right)... 42

Figure 24 Height difference of the DSMs from 2014-2017 (left column) for the erosion intensities (top) and vegetation classes (bottom) (N = 12,891); examples of vegetation classes a) - vegetation-free soil (I), b) - sparse grass vegetation (II), c) - area-wide grass/herb vegetation (III) from the 2017 orthophoto (right column); the newly constructed glide snow frames are visible as triangular features in (I). 43

Figure 25 Detailed view of orthophotos from the lower burnt area of the Hochmahdkopf in 2014 (left) and 2017 (right), illustrating the rapid successional development in severely burnt areas. 44

Tables

Table 1: List of the area distribution of the reference area damage (ha). 16
Table 2: SAR backscatter behavior for the two polarizations VV and VH of all four areas. 16
Table 3 Overview of satellite products for forest monitoring such as tree cover, storm damages and drought effects 49
Table 4 Overview of satellite products useful for the exploration of natural hazards 49
Table 5 Data hubs to access satellite imagery for various applications 47
Table 6 Satellite data access points for remote sensing specialists 52
Table 7: Technical specifications of the Mentor UAS (Adams et al., 2016) 54
Table 8: Properties of UAS-flights on 15 November 2015. 55

Introduction

Remote sensing in the forest has a very long tradition. The view from above facilitates orientation and allows views that would never be possible from the ground. Dividing the forest into stands or treatment units would be much more difficult and time-consuming without e.g. aerial photography - in some cases not possible at all. Detailed interpretation keys have been and are being used to try to make the interpretation consistent and reproducible. The increasing availability of digital data and products from remote sensing has paved the way for automated procedures. A great deal is already operational. For example, in addition to digital orthophotos, which are common tools in the age of Google Earth or Bing Maps, digital 3D vegetation elevation models are also available to visualize stand heights and forest structures, to use them as a basis for planning or to derive 3D features over large areas and longer time periods.

However, the data already available today make much more possible. Many forest functions can be quantified using remote sensing methods. Wood supply as a resource can be measured to a large extent by height, biodiversity by the vertical and horizontal forest structure and protection by crown density, distribution of trunks and tree species. Some features cannot be measured directly, but indirect models must be applied.

Data from satellites are very easily available today, but since several years data hosts and remote processing options have been popping up and it might be difficult to keep track of which resources and processing servers might be best for various user needs. We therefore give a brief overview for three different types of users (forest, natural hazard and remote sensing specialists) and where satellite data are accessible. The spatial resolutions are comparable to those of aerial photographs. Satellite images are available today with sub-meter ground resolution. Besides the ever-increasing spatial resolution of satellite data, the temporal resolution is also improving. The opening of image archives and the free and very easy access to satellite data (e.g. Landsat archive, Sentinel) has stimulated research and development work. Such time series, e.g. dating back to the 1990s for Landsat, have great potential for monitoring and analyzing changes, disturbances and interventions at global and regional level. One example is the "Global Forest Change" project, which makes changes in forests freely available online with a temporal resolution of one year and a spatial resolution of 30 m (Hansen et al 2013).

Excellent results of case studies sometimes have to be put into perspective for large area applications. The intensive exchange between research and practice is indispensable. Today, there are many possibilities for practical applications to integrate remote sensing into daily work processes.

In the report on remote sensing methods for the identification and permanent monitoring of forest disturbances, different sensors on different platforms are discussed. Forest disturbances are understood as both abrupt changes (e.g. storm, fire, avalanches) and long-term changes (e.g. changes/damages caused by drought, insect infestation, frost).

The report presents and discusses the potentials and applications of the various platforms. For small-scale damage, unmanned aerial vehicles (UAVs) are very efficient and flexible platforms. With simple sensors, such as RGB cameras, data on small-scale events can be captured very quickly. The benefit of other sensors (CIR, LiDAR, spectrometer) will be discussed. If larger areas are affected by disturbances, it makes more sense to use helicopters and airplanes. The pro and cons of cameras (RGBN) and LiDAR are discussed as sensors. For larger areas, data from satellites with a very high temporal and acceptable spatial resolution are available today. Multispectral data from Sentinel-2ab (>= 10m x 10m) are available at intervals of 3-5 days. The advantages and disadvantages of multispectral sensors (intuitively interpretable but no data in cloudy conditions) are discussed. Alternative methods with RADAR (Sentinel-1ab) are presented.

The different approaches are presented in the case-study chapter. Examples on ongoing work and recent studies with different platforms and sensors are presented:

1. Rapid assessment of Storm Damages with Sentinel-1
2. Analysis of drought effects after the dry/hot summer 2018 with Sentinel-2
3. Fungal infestation of Pinus nigra in Lower Austria with UAS
4. Avalanche forest damage in Tyrol with UAS

A last chapter will present an overview of free and paid access and platforms to Earth observation data useful for forest degradation, disturbances and natural hazard monitoring.

Satellites

The accessibility to satellite data for forest and natural hazard monitoring has skyrocketed in the last decade, not least because the European Space Agency (ESA) has an open access policy. For monitoring services, we may differentiate optical and radar systems.

Optical Earth Observation data sets that are useful for forest and natural hazard monitoring have in general a high resolution between 5 and 30 m. Very high resolution (VHR) resolution sensors have a pixel size of < 2 m and the capacity to give very precise information on forest degradation or the details of a natural hazard deposit. However, the repeat cycles might either be cost intensive, as data acquisition might just happen on demand. Medium to coarse resolution sensors with 30 to > 60 m ground resolution have lower costs and are often open access data still offering the potential for forest monitoring. Landsat satellites deliver multispectral data since 1972 and are available without restrictions from the USGS (United States Geological Survey). The new generation of Landsat 7 and 8 are available on e.g. the Google Earth Engine without restrictions. ESA follows also a strict open access policy for the optical multispectral Sentinel-2 satellites and the Synthetic Aperture Radar (SAR) satellites Sentinel-1A/B.

Optical satellites cover wavelengths between 400 and 13000 nm and are given in detail in Tables 3-6. Satellite data are processed with image processing methods and thus valuable products for forest monitoring are gained (Hirschmugl et al. 2017). Different indices can be used for forest change monitoring: normalized difference vegetation index (NDVI), enhanced vegetation index (EVI), normalized burnt rate (NBR), and the soil-adjusted vegetation index (SAVI) (Hirschmugl et al. 2017). Changes in forest crown cover are mapped based on mapping methods developed over the last 10 years (Banskota et al. 2014, Hansen et al. 2014).

Radar satellite data are available since the 90ies, but with the recent launch of Sentinel-1A/B satellites in 2014 and 2016 with a repeat cycle of only 6 days, the potential to use Synthetic Aperture Radar (SAR) offers a very high potential to use radar data for forestry applications (Kellndorfer 2019, Siqueria 2019). The SAR-principle is based on actively transmitting electromagnetic microwaves and analyzing its echo. SAR has the advantage that it provides data during the night, even when it is cloudy, though it is not completely weather insensitive and atmospheric signals and terrain have to be considered. SAR platforms deliver data with high spatial resolution between <1m and 100 m. Sentinel-1 products range from Spot (1 m), via Stripmap (3-5 m) to ScanSAR (30-100 m). The phase of the reflected signal is related to the distance of the sensor to the target in different frequency bands (X-, C-, L-bands) (Meyer 2019). The radar signals penetrate deeper into surfaces as the wavelength of the sensor increases. For forest areas, this means that X-band SAR sensors usually scatter at the tops of the trees, while C- and L-band signals penetrate increasingly deeper into the vegetation volume (Meyer 2019). Therefore, longer wavelengths (C- and L-band) should be used for the characterization of vegetation than for the characterization of natural hazards (X- and C-band).

SAR datasets have been used to Monitoring, Reporting and Verification (MRV) in various countries and the combination of different platforms with different bands (X, C or L-band) offer yet to explore options such as capturing forest stand heights, canopy characterization biomass and forest structure (Flores-Anderson et al. 2019, Dostálová et al. 2016). Major challenges of the SAR method are data storage and processing capacities and the lack of consistent workflows to process data not just for pilot regions.

Unmanned Aerial Systems

Advances in recent years in the fields of aircraft construction (light weight construction & engine development), navigation (GNSS – Global Navigation Satellite System & IMU – Inertial Measurement Unit) as well as mechatronics in general (mechanics, electrical engineering & informatics) and digital photogrammetric software design in particular, have given rise to the development of **Unmanned Aerial Systems** (UAS) (Briese et al., 2013). The term UAS is used here according to the recommendation by the International Civil Aviation Organization; other denominations include Unmanned Aerial Vehicle (UAV), Remotely Piloted Aircraft System (RPAS) or drone. UAS is the collective designation for an aircraft and its associated elements which are operated with no pilot on board (ICAO, 2020). According to the classification suggested by Watts et al. (2012), the type of aircraft may range from Micro or Nano Air Vehicles (MAV/NAV) with a typical flight time of 5-30 min, operating at very low altitudes (< 330 m), to High Altitude, Long Endurance (HALE) platforms, operating at altitudes of 20,000 m and more and with flight times of > 30 h, used for both civil and military missions. In the context of this deliverable, the term UAS refers to the scientific use of different types of Low Altitude, Short Endurance (LASE) aircraft with a typical weight of < 5 kg, flight times of 20-40 mins and a wing span of < 3 m, optimized for easy field deployment / recovery and transport. The three main platforms available within this definition of UAS include fixed-wing aircraft, helicopters and multicopters.

In general, UAS are able to bridge the gap between full-scale, manned aerial, and terrestrial, field-based observations (Briese et al., 2013; Rosnell & Honkavaara, 2012). The primary advantages of the LASE UAS include the possibility for flexible, cost-effective, on-demand mapping missions with multiple sensors at an unprecedented level of detail (ground sampling distance (GSD) of few centimetres or millimetres, depending on camera properties and flight height) (Ryan et al. 2015). Due to the fact, that UAS are operated at lower altitudes, medium / high level clouds or haze also less influences them. Due to their small size however, they can only be operated under favourable weather conditions (e.g. low wind speed, good visibility). From a scientific point-of-view, UAS offer the advantage of allowing a flexible matching of the required spatial resolution and sensor type to the specific application, i.e. research question at hand (Colomina and Molina 2014; Lucieer et al. 2014); this is reflected in a wide range of recent reports on UAS-related forestry applications (Tang & Shao, 2015), which include: Forest surveying (Paneque-Galvez et al., 2014; Koh & Wich, 2012); canopy gap mapping (Getzin et al., 2012); forest wildfire tracking (Lechner et al., 2019b; Ambrosia et al., 2011; Hinkley & Zajkowski, 2011); forest management (Wang et al., 2014; Felderhof & Gillieson, 2011). Further applications of UAS include monitoring: soil erosion (e.g. D'Oleire-

Oltmanns et al., 2012), landslide and debris flow (e.g. Niethammer et al., 2012; Sortier et al., 2013), slope deformations (Hormes et al. 2020), archaeology (e.g. Verhoeven, 2011), seasonal snow (e.g. Bühler et al., 2016), geomorphology (e.g. Hugenholz et al., 2013) and hydrology (e.g. Molina et al., 2013). A detailed summary of civil UAS applications is supplied by González-Jorge et al. (2017).

The development of novel computer vision techniques and their implementation into a wide range of software packages, have considerably reduced the requirements for the recorded data (Vander Jagt et al. 2015; Turner et al. 2012). Processing the UAS imagery is therefore usually performed with off-the-shelf or custom structure-from-motion photogrammetry software; for a comprehensive review on available software options, see Nex and Remondino (2014) or Colomina and Molina (2014). Standard outputs are orthophotos, digital surface models (DSM) and (RGB-)coloured 3D dense point clouds (DPC). DSMs generally refer to the height of the terrain, buildings or vegetation, captured in the scene (Adams et al. 2016). The DSM is interpolated from DPC, generated with multiview stereo reconstruction as part of the photogrammetric workflow (Vander Jagt et al., 2015). When calculating terrain height changes (e.g. when mapping mass movements in forested terrain) all objects on or above the terrain should be removed. This is typically achieved by classifying the DPC into ground and non-ground points, and subsequently generating a digital terrain model (DTM). The use of photogrammetric DTMs may be limited in densely forested areas, as only few ground points are recorded. Therefore, masking out the process area before calculating terrain height change may avoid potential errors (Tang & Shao, 2015).

Rapid assessment of Storm Damages with Sentinel-1AB

This study was conducted by Marius Rüetschi, Lars Waser, David Small and Christian Ginzler as a collaboration between the Federal Office for the Environment (FOEN) and the Swiss Federal Institute for Forest, Snow and Landscape Research WSL (Rueetschi et al. 2019).

Introduction

After a major storm event, it is of interest to quickly gain an initial overview of the damage caused to the forest. Satellite-based remote sensing is ideally suited for this purpose, as it can provide such an initial overview after a short time, at relatively low cost and for a large area (e.g. the whole of Switzerland). Studies show that satellites with optical sensors are well suited for this. Damage can be located with a high degree of accuracy (Baumann et al., 2014; Einzmann et al., 2017). This has also been shown specifically for Switzerland in a project on forest monitoring with sentinel 2 satellite images financed by the Federal Office for the Environment (FOEN) (Weber and Rosset, 2019). Optical sensors have the disadvantage, however, that it is not possible to record the earth's surface when it is cloudy. Therefore, a guaranteed and rapid data availability after a storm event is not given. Since most large-scale storm events in Switzerland occur in the autumn and winter months (Usbeck, 2015), when the probability of cloudiness is high, the availability of evaluable satellite images shortly after the event cannot be guaranteed. Therefore, it was investigated whether there are possible alternatives and synergies with Synthetic Aperture Radar (SAR) data, which record data of the earth's surface independent of cloudiness and therefore have a high recording frequency. An overview of the frequency of the two SAR satellites Sentinel-1A/B is shown in Figure 1. The lowest frequency of at least 2 SAR recordings within 6 days occurs in two wedges over Western Switzerland and Eastern Switzerland. Otherwise, at least 3 SAR images within 6 days are available for the whole of Switzerland.

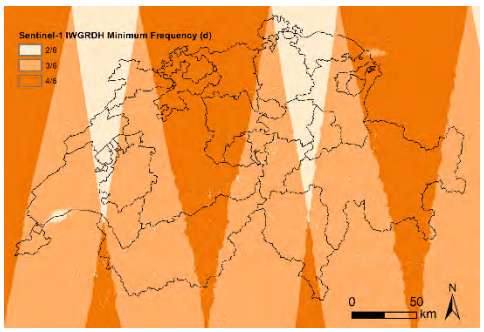

Figure 1: Frequency map for the minimum number of SAR images of Sentinel-1.

Based on a thunderstorm in the northern canton of Zurich on 2 August 2017 and the "Xavier" autumn storm of October 2017 in Mecklenburg-Western Pomerania, a project at the WSL in cooperation with the University of Zurich developed a method for generating indications of extensive storm damage in 2018 (Rüetschi et al., 2019). For this purpose, data from the Sentinel-1 satellite pair, which are equipped with SAR sensors, are used. The method is based on a novel combination of several individual SAR images developed at the University of Zurich (Small et al., 2019), which reduces the noise to such an extent that short-term and larger changes in SAR backscatter in the forest can be perceived as indications of storm damage.

Within the framework of this project, it was investigated whether this method, which was developed for events in leafy conditions, can also be applied to unleafed conditions in winter. Supraregional storm damage usually occurs in winter with unsuitable conditions for satellite or aerial photography with optical sensors (Usbeck, 2015). Prominent examples are the storms "Vivian" in 1990, "Lothar" in 1999 and "Burglind" in 2018, making a potential application of the method with SAR data all the more promising. However, since factors such as snow and temperatures below freezing point have a strong influence on SAR backscatter in winter, their influence on a successful application was investigated within the scope of this project.

Data from the most recent major storm events in Switzerland were collected. Subsequently, the following possible influencing factors on SAR backscatter in different study areas (depending on the availability of corresponding reference data) were analyzed in order to explore possible further development potential of the method:

- Temperature
- Precipitation
- Lying snow
- Water content in snow
- Vegetation height
- Crown coverage
- Degree of forest mixture
- Slope
- Aspect

On the basis of these findings, the method of Rüetschi et al (2019) was then further developed. The accuracy achieved with the revised method in the detection of windthrows is shown. The accuracy is shown as a function of the number of SAR images (= time required after a storm) and of the minimum size of the damage areas to be detected. In addition, the values of the newly developed area proxy are briefly discussed. Different ways to publish the data to potential stakeholders are shown.

Study areas and data

In order to cover as many different storm events as possible, mapped references from various storm damage cases in Switzerland were collected. The references come from different times of the year and range from topographically flat (e.g. Central Plateau) to complex areas (e.g. Alps). Storm damage references could be obtained from the following areas and storms:

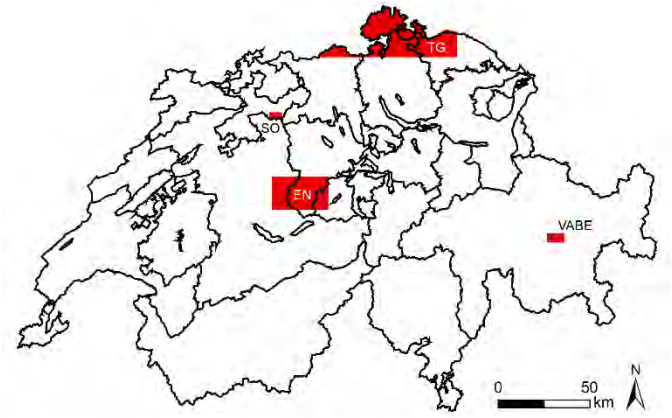

Figure 2: Localization of the various storm damage cases processed

Since at least 5 SAR images were available for all of the study areas before and after the storm event, the entire analyses were subsequently performed on 5 SAR images for comparison with Local Resolution Weighting (LRW) composites. The LRW composites were calculated in two phases by David Small at the University of Zurich (UZH) using a UZH algorithm. In a first phase, the individual SAR images were corrected both geometrically and radiometrically using a digital elevation model (Federal Office of Topography Swisstopo, 2018) (Small, 2011). In a second phase, in order to reduce the noise typical in individual SAR images, two LRW composites were calculated from these 5 SAR images for before and after the respective storm event (Small et al., 2019).

Reference data were available on the basis of terrestrial mapping or the interpretation of high-resolution remote sensing data (

Table 1).

Table 1: List of the area distribution of the reference area damage (ha).

Event	Date	Area	0-0.5	0.5-1	1-1.5	1.5-2	2-2.5	2.5-3	>3	Total	Type of ref.
Thunderstorm	02.08.17	TG	38	12	4	2	5	2	1	64	Field
Burglind	04.01.18	EN	17	21	8	4	3	0	2	55	Planet
Burglind	04.01.18	SO	6	12	2	4	0	3	8	35	Field
Vaia	30.10.18	VABE	47	6	2	0	1	0	2	58	Planet
Total			**122**	**55**	**16**	**12**	**10**	**5**	**14**	**234**	

If we look at the differences in SAR backscatter δ between the forest and the windthrows references of the different areas, we see that the same effect can be observed in all areas, on which the method is based. The δ values for windthrows are generally higher than for forest (Table 2, second last column). The fact that the δ values from the forest are also positive for all areas may be because the damage areas are all included in the class 'forest'. In addition, there are also potentially unmapped damages in each area.

Likewise, the variance of the SAR backscattering difference δ is larger within the windthrows areas (Table 2, last column). Another interesting observation regarding the variance (or standard deviation) is the lowest standard deviation in the area with the flattest topography (DE). The more complex the area, the higher the standard deviation. From this, it can be concluded that an extraction of wind casts based on the differences in the SAR backscatter difference δ is more difficult and less accurate in topographically more complex areas. Within the scope of this project, therefore, an attempt was made to find explanations for the observed differences.

Table 2: SAR backscatter behavior for the two polarizations VV and VH of all four areas.

Area	Pol.	Forest area			Windthrows			Difference	
		mn δ [dB]	sd δ [dB]	n	mn δ [dB]	sd δ [dB]	n	mn δ diff [dB]	sd δ diff [dB]
SO	VV	0.3	1.35	71751	0.87	1.38	8963	0.57	0.03
SO	VH	0.33	1.33	71751	0.86	1.38	8963	0.53	0.05
TG	VV	0.05	1.58	80354	0.5	1.78	4101	0.45	0.2
TG	VH	0.31	1.6	80354	0.97	1.81	4101	0.66	0.21
EN	VV	0.24	1.87	1135451	0.4	1.93	4104	0.16	0.06

EN	VH	0.42	1.97	1135451	0.58	1.96	4104	0.16	-0.01
VABE	VV	0.31	1.62	18492	0.45	1.68	3070	0.14	0.06
VABE	VH	0.32	1.62	18492	0.3	1.7	3070	-0.02	0.08

Results

Three factors had a decisive influence on the quality of the method: the height of vegetation, the content of liquid water within the snow cover and the topography.

- Only from a vegetation height of 15 m reliable differences in radar backscatter between intact forest and windthrows can be detected. Thus, relevant stands can be covered.
- Liquid water within the lying snow cover influences the radar backscattering so strongly that it makes the application of the method in areas with wet snow impossible.
- Radar sensors do not reliably measure the backscatter in areas with steep slopes (> 60°) for reasons of recording geometry. This corresponds to a forest area of approx. 5% in Switzerland as a whole.

The method was developed on the basis of these findings. Indications for storm damage in stocked areas of 15 m and above are shown. In the "Burglind" case, large parts of the foothills of the Alps were affected by wet snow, so these areas were excluded from the evaluation. In the future, this influence should be specifically investigated in order to make appropriate adjustments to the method, so that indications of storm damage can also be generated in these areas. The 5% of forest areas from which no reliable radar measurements can be made were also excluded from the procedure.

Presentation and dissemination of results

The result of the procedure is a reference card for storm damage. In order not to suggest an exact mapping with the result, the clues are presented in generalized form as a grid of hectares or as point clues in the form of coordinate pairs. Figure 3 shows an example for the representation of the point clue. An automatic cluster algorithm adapts the representation of the points according to the selected room section.

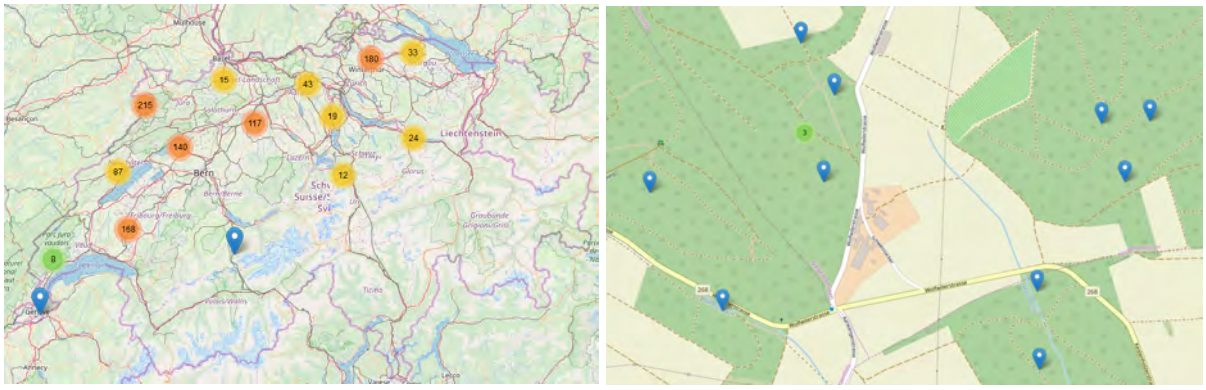

Figure 3: Representation of the coordinate pairs of indications for storm damage with a minimum area of 0.5 ha. On the left, a general overview of Switzerland after "Burglind", on the right, a greatly enlarged section near Kestenholz (SO). The interactive result for the whole of Switzerland can be accessed at https://tinyurl.com/Hinweis-Cluster. © Open street map.

Analysis of drought effects after the dry/hot summer 2018

This study was conducted by Achilleas Psomas and Charlotte Steinmeier as a collaboration between the Federal Office for the Environment (FOEN) and the Swiss Federal Institute for Forest, Snow and Landscape Research WSL (Psomas et al. 2019).

Introduction

In 2018, Central and Northern Europe – including Switzerland – experienced one of this region's most severe droughts of the last century which in some areas was worse than the drought of 2003 (Buras et al. 2019). In Switzerland the spring and summer months of 2018 were characterized by a unique combination of low precipitation and high temperatures which had a significant effect on water supplies of lakes and rivers, glacier melting and increased forest fires hazard. In particular, 2018 summer temperature differences were 3.5 °C higher and precipitation 40% lower compared to the long term average (Brun et al. 2020). The effects of the drought were especially severe in the north-eastern part of Switzerland (Brunner et al. 2019) and on forests ecosystems in these areas. Large areas of forest showed premature canopy browning with species like Fagus sylvatica and Picea abies (amongst others) showing signs of stress as a response to the drought. While a number of studies exist that analyse the drought of 2018 (Pestalozzi 2019) its direct impacts on forest ecosystems of Switzerland and their subsequent effects in 2019 are still unexplored.

In this study we wanted to explore the potential of remote sensing and in particular of ESA's Sentinel-2 mission to a.) map the areas of forest under drought stress in 2018 for the north-eastern part of Switzerland and investigate which forest mixture groups (deciduous-needleleaf gradient), tree species and tree ages groups were affected the most. We also aimed at b.) investigating the potential effects of the 2018 drought in forest areas in 2019 by using remote sensing to detect and map forest disturbances in 2019. How much of these could be attributed/linked to the drought

of 2018? This work was performed at the scale of the whole north-eastern part of Switzerland but also at the scale of Cantons (Figure 4).

Remote sensing data

The remote sensing data used for this study were optical Sentinel-2 MSI (Drusch et al. 2012) covering the whole extent of the study region. Sentinel-2 is a wide-swath, high-resolution, multi-spectral imaging mission by ESA for monitoring vegetation cover, soil and water cover. Sentinel-2 Level-1C and Level-2A data were used. Level-1C data are radiometric and geometric corrected Top-Of-Atmosphere products and Level-2A are Surface Reflectance data. The corrections include orthorectification and spatial registration on a global reference system (combined UTM projection and WGS84 ellipsoid) with sub-pixel accuracy. Sentinel-2 data are delivered in tiles of 100×100 km. From the eleven tiles covering the extent of Switzerland (

Figure 4), four were required to cover the study region (32TLT, 32TMT, 32TNT, 32TNS).

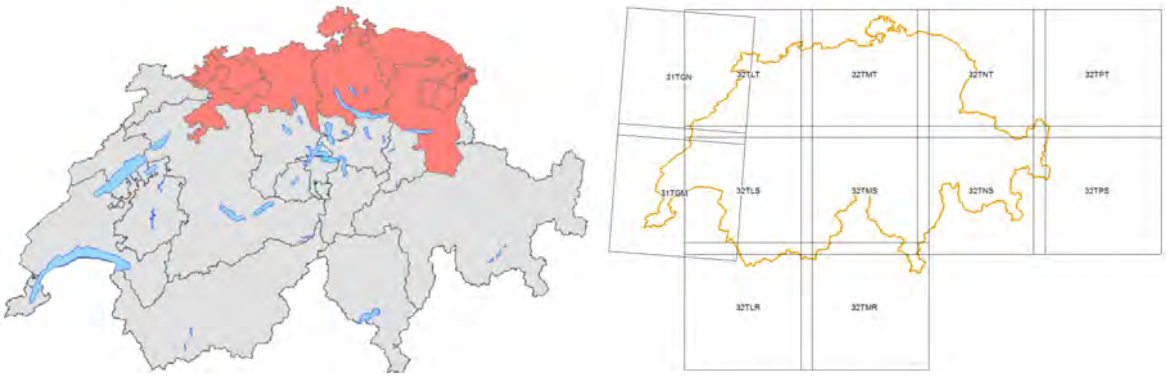

Figure 4: Study area (left) and Sentinel-2 tiles covering Switzerland (right)

Initial analyses included removing cloud-contaminated pixels. Upon investigation of the early results, we realized that the cloud mask provided by ESA did not sufficiently remove all cloud pixels. We thus decided to continue the analyses with Sentinel-2 tiles that had cloud coverage of 50% and below. All analyses were performed on the Google Earth Engine (GEE) (Gorelick et al. 2017). GEE is a cloud-based geospatial-processing platform for executing large-scale spatial data analysis with multi-petabyte catalog of satellite imagery, climate, demographic, and other global or regional vector datasets available.

Mapping drought stress on forests

To map drought stress on forests we used Sentinel-2 Level-1C data to calculate the Normalized Difference Water Index (NDWI) (Gao 1996) for the extent of the study region. NDWI is an index derived as the normalized difference between the Near-Infrared (NIR) and Short Wave Infrared (SWIR) channels of the electromagnetic spectrum. The potential of NDWI as a proxy of vegetation water content and its usefulness for drought monitoring has been shown in literature (Liu et al. 2004, Gu et al. 2008). The reflectance of the SWIR channel is linked to changes in the vegetation

water content and the mesophyll structure of vegetation canopies. The NIR reflectance is determined by leaf internal structure and leaf dry matter content but not by water content. By combining the NIR with the SWIR channels spectral differences due to leaf internal structure and leaf dry matter content are minimized, and we thus improve the accuracy in the retrieval of vegetation water content

In this study we calculated the anomalies of NDWI for 2018 in comparison to a base period of normality defined as years 2016-2017. In particular we calculated NDWI anomalies for the reference period between July 20th (DOY: 201) and August 31st (DOY: 243) when the drought had reached its most severe period and the effects of it started being even visually visible on forests. While Sentinel-2 data exist since 2015 only years 2016-2017 were used as a base/normality period to 2018. Year 2015 was intentionally excluded due to very warm and dry conditions that also led to a drought across large parts of Europe and Switzerland (Ionita et al. 2017).

A total of 73 (2016-2017) and 62 (2018) Sentinel-2 tiles were considered for the analyses. For each tile, the NDWI was calculated at 10m resolution using the NIR (Band 8) and SWIR (Band 11) of the Sentinel-2 sensor. Then for the reference period of 2016-2017 and for 2018 the median was calculated using all the available data for the respective years. Using the median was a better representation of the true value of the pixel compared to the mean since data might still contaminated with rather high or low values like remaining clouds and their shadows. Finally, the NDWI anomalies for 2018 were as shown in Equation 1.

$$NDWI_{\text{anomaly}} = \frac{NDWI_{2018} - NDWI_{Reference\ Period}}{NDWI\_SD_{Reference\ Period}}$$

The NDWI anomalies were calculated in standard deviation units that ranged typically from -4 to +4. Negative values represented areas with lower vegetation water content in comparison to the reference period. Values between -1 to +1 were considered normal while values larger than 1 or lower than -1 higher/lower than normal.

Mapping forest disturbances in 2019

In order to investigate the potential effects of the 2018 drought on forest areas, we established a two-step analysis. First we identified all forest areas that were healthy in 2018. Then we compared which of these areas had transitioned from a healthy to a non-healthy status in 2019 and finally examined what the water stress status (NDWI anomaly) of these was in 2018.

To establish healthy forest areas in 2018 we collected all available Sentinel-2 Level-2A data for the period between April 15th (DOY: 105) and June 30th (DOY: 181). We selected this period to avoid any significant effects that the prolonged drought could have on the trees, as we could observe later in 2018. A total of 54 Sentinel-2 tiles were used to calculate the median Normalized Difference Vegetation Index (NDVI) (Broge and Leblanc 2001) at 10m resolution using the Red (Band 4) and

NIR (Band 8) bands of the Sentinel-2 sensor. All forest areas with an median NDVI value higher than 0.4 during the period April 15th-June 30th 2018 were considered healthy (Jensen 2007).

We defined forest areas that transitioned from a healthy to a non-healthy status in 2019 as area where large disturbances (forest timber logging and/or forest mortality) took place between 2018-2019. To identify these types of disturbances we collected all available Sentinel-2 Level-2A data for the period between April 15th (DOY: 105) and June 15th (DOY: 166) for 2018 and 2019 respectively. We selected this period, which is rather early in the season, since we realized that in many areas where forest was removed in 2019 the effect of the newly growing herb/bushy vegetation had a significant effect on the remote sensing signal. In particular, the more we progressed into the growing season the accumulating biomass of herbs/bushes led to a spectral signal which resembled that of a forest. Thus we restricted the period to mid of June (DOY: 166)

A total of 50 (2018) and 22 (2019) Sentinel-2 Level-2A tiles (with cloud coverage less than 50%) were used to calculate the Normalized Burn Ratio Index (NBR) (Key and Benson 2006) at 10m spatial resolution using the NIR (Band 8) and SWIR (B12) of the Sentinel-2 sensor. We selected NBR versus NDVI or any other index since previous research (Cohen et al. 2010, Shimizu et al. 2017) has indicated that NBR is more sensitive in disturbance detection. We used very high-resolution satellite imagery to visually identify forest disturbances across the whole extent of the study region. Images were obtained from the PLANET sensor constellation (www.planet.com) at 3-5m spatial resolution, which allowed for the comparison between 2018 and 2019. After visual inspections of forest disturbance areas we decided that a reduction larger than 50% on the value of the value of NBR in 2019 relative to that of 2018 was a good indicator of forest timber logging and/or forest mortality in our study region.

As a final step we identified which forest areas were healthy in 2018 and at the same time had deviation of NBR larger than the established threshold between 2018-2019 and used these areas for further analyses. To ensure reliability of the results only pixels that had at least three Sentinel-2 observations during each of the given periods in 2018 and 2019 were considered for further analyses.

Additional datasets

All analyses in this report were restricted to forest areas across the study region. Available forest mask data from the National Forest Inventory (NFI) at 1m spatial resolution (Waser et al. 2015) were aggregated to 10m to match the resolution of the Sentinel-2 data. An example of the forest mask dataset is given in Figure 5.

Figure 5: Example of the forest mask (right) used in this study around the city of Schaffhausen. Areas of forest not covered by the mask (top right, left bottom) are outside the study region.

Since we wanted to investigate which forest mixture groups (deciduous-needleleaf gradient) and forest species were a.) under drought stress in 2018 and b.) the 2019 disturbances took place, we used two additional datasets. The first one was the countrywide mapping NFI dataset of broadleaved and coniferous trees in Switzerland (Waser et al. 2017). In particular, it provided information about the proportion of deciduous trees at the scale of 25m pixels. Its values range from 0-100% where 0 indicates 25m pixels where 0% is covered by deciduous and 100% by needleleaf forest species and 100 indicates that 100% of the pixel is covered by deciduous species. First, this dataset was resampled to 10m to match the resolution of the Sentinel-2 data. Then, we reclassified it into four new classes. Pure needleleaf pixels (0-10% proportion deciduous), needleleaf-dominated (10-50% proportion deciduous), deciduous-dominated (50-90% deciduous proportion) and pure deciduous pixels (90-100% proportion deciduous). An example of the dataset is given in Figure 6.

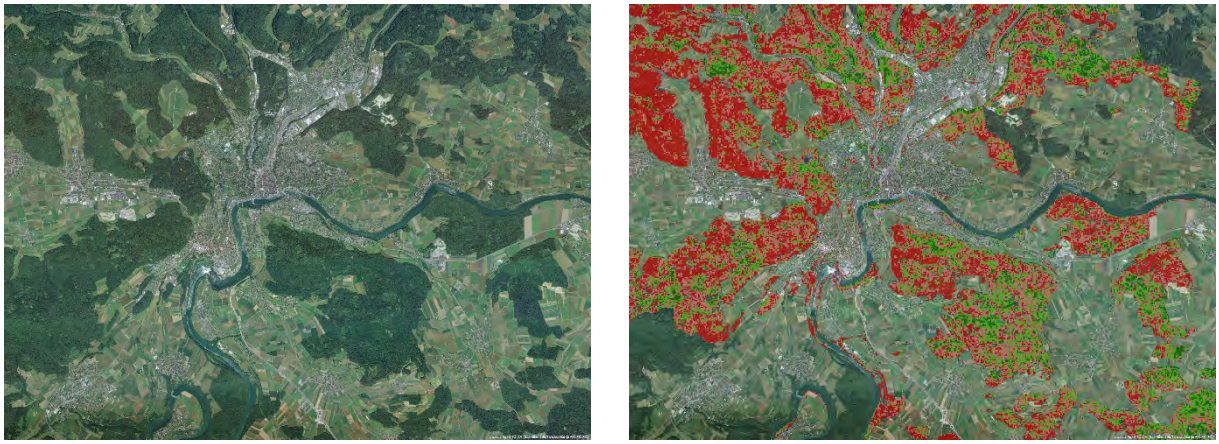

Figure 6: Example of the forest mixture dataset used for this study around the city of Schaffhausen. Darker green colors represent pure needleleaf forest areas, light green needleleaf-dominated, light red deciduous-dominated and dark red pure deciduous forest areas.

We furthermore wanted to investigate which forest species were affected by the drought of 2018 and disturbances were detected in 2019. Currently there is no available wall-to-wall dataset at the species level for Switzerland that is based on actual observations. Thus, we used a dataset (Wüest et al. 2020) where spatial distribution of forest species were modeled using species distribution models (SDMs) (Guisan and Zimmermann 2000). These maps represented the potential distribution of forest species, meaning they showed where a species could theoretically exist without taking into account factors like competition from other species or human management. For this work, we selected a set of deciduous and needleleaf forest species whose modeling accuracy was high (True Skill Statistic > 0.75) and were abundant in the study region, namely: *Acer campestris Acer platanoides*, *Fagus sylvatica*, *Fraxinus excelsior*, *Picea abies*, *Pinus sylvestris*, *Quercus petraea* and *Quercus robur*. An example of this dataset is given in Figure 7.

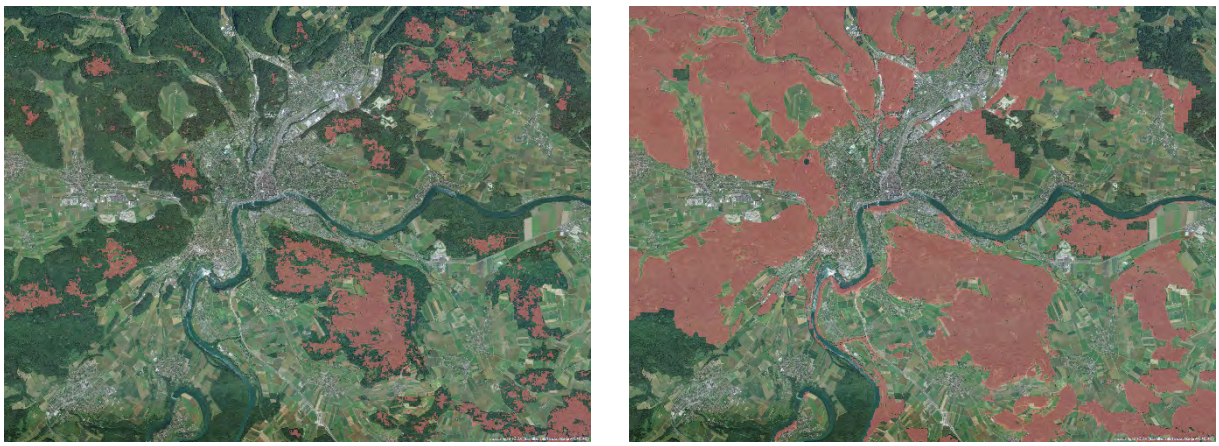

Figure 7: Spatial distribution (in red) of Picea abies (left) and Fagus sylvatica (right) around the area of Schaffhausen. Notice that since these data represent the potential spatial distribution of the species they are not mutually exclusive. Thus, a significant spatial overlap can be observed.

Finally, to investigate if trees of certain age were more prone to drought stress and forest disturbances we used the vegetation height model (VHM) dataset from the NFI, available at 1 m for the extent of the study region (Ginzler and Hobi 2015). Trees with a height between 3-15 m were considered young in age, trees between 15-25 m adult and trees with height above 25 m mature/old. The VHM was first aggregated to 10m in order to match the resolution of the Sentinel-2 remote sensing data and then was reclassified to the three classes mentioned above. An example of the VHM dataset is given in Figure 8.

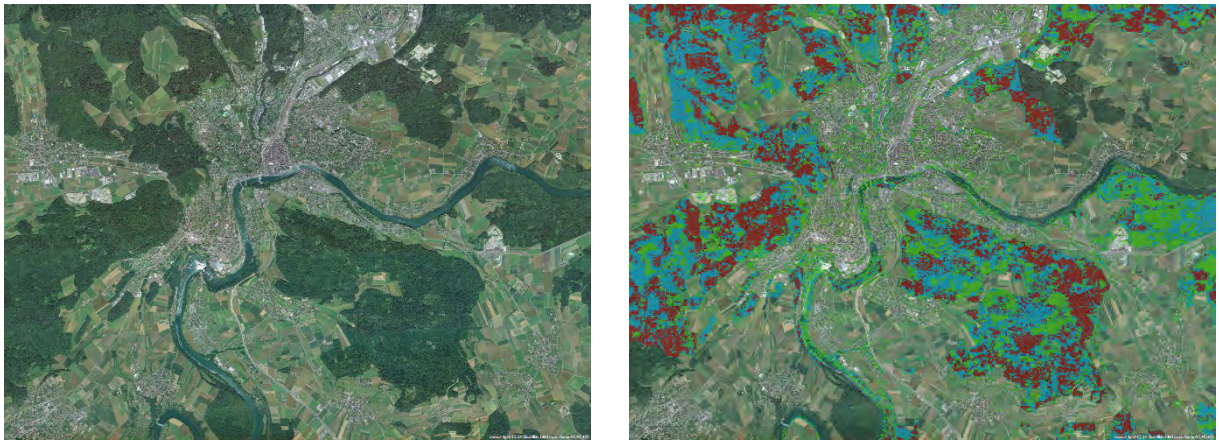

Figure 8: Example of the vegetation height dataset used for this study around the city of Schaffhausen. Green colors indicate trees with a height between 3-15 m, blue trees with a height between 15-25m and red color trees higher than 25m.

Results

Drought stress on forests

The yearly NDWI anomalies for 2018 for the extent of the study region are shown in Figure 9. Areas that had NDWI difference to the base/normality period (2016-2017) lower than 2 standard deviations are depicted in red and are considered to be under severe water stress.

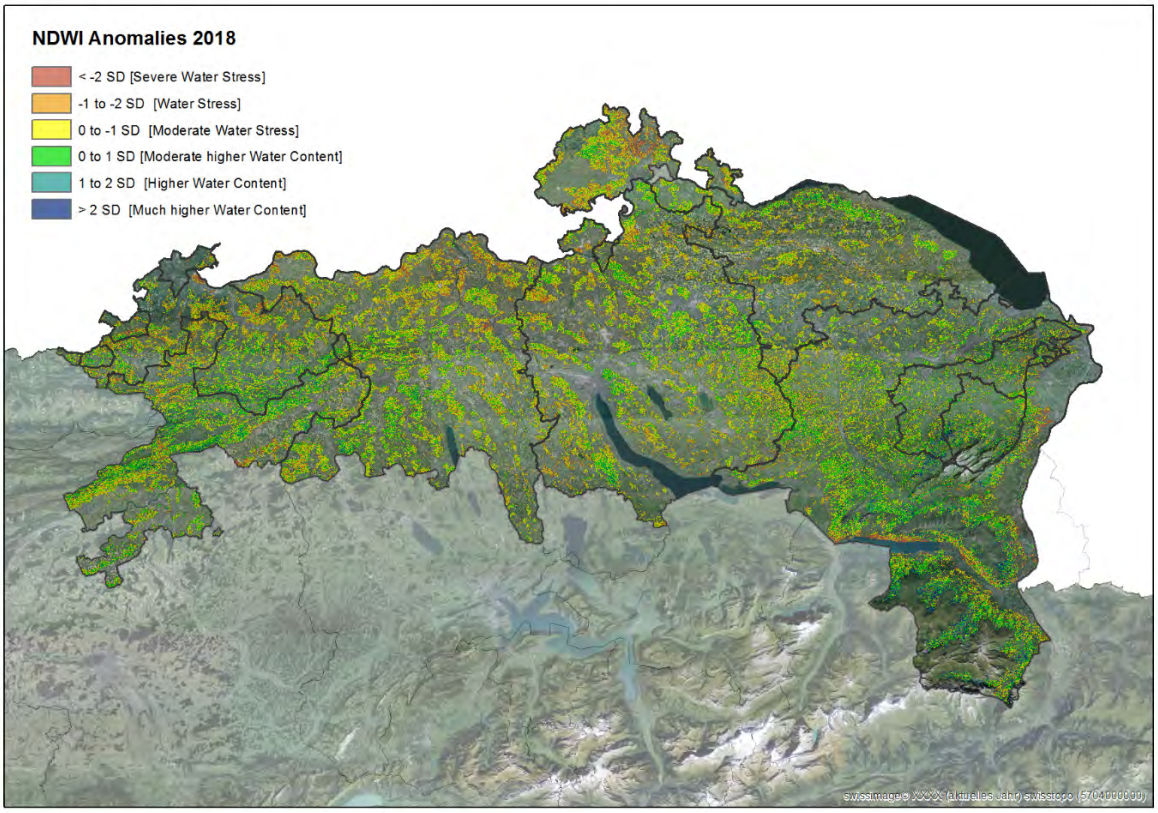

Figure 9: NDWI anomalies for 2018 for the extent of the study region.

Looking at the map we can observe that even at this coarse scale large forest areas in the regions of Schaffhausen, northern Aargau and Walensee (amongst others) are under severe water stress. For the remaining of this document we will report only forest areas that were under severe water stress (NDWI anomalies <2 SD to 2016-2017).

A total of 33'810 ha of forest were found to be under severe water stress during the period July 20th and August 31st 2018 that accounted for 12% of the total forest in the study region. More detailed results at the level of different cantons are presented in Figure 10. We can see that while canton St. Gallen had the largest area of forest under severe water stress (7'608 ha) this accounted for only 11.7 % of the total forest area. In contrast, cantons like Schaffhausen had smaller areas under severe water stress (2'315 ha) but this accounted for 17.5 % of the total forest area. An interesting situation occurred at the canton of Basel-Stadt where 36 % of the total forest area was under severe stress. However, this area was only 189 ha out of the 525 ha of available forest and overall minimal with respect to the total forest area under stress across whole the study region (0.56 %). Overall, cantons with large areas of forest had equally large areas of forest under severe water stress whereas the canton of Zurich was the one with the smallest percentage (10.5 %).

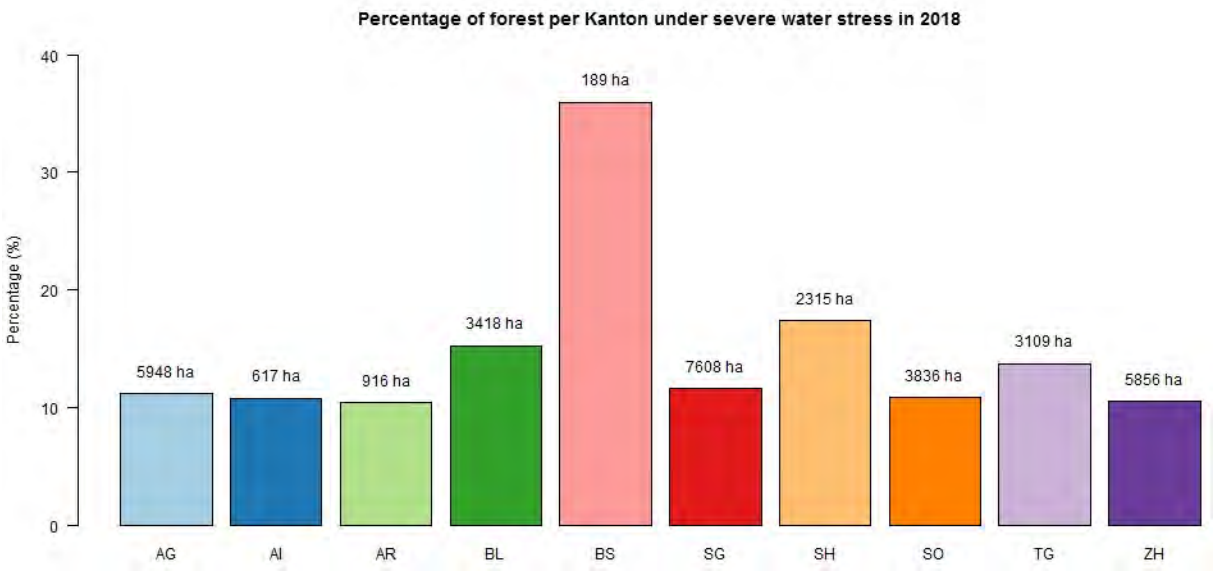

Figure 10: Percent of total forest area under severe water stress per canton within the study region. The numbers on top of the bars represent the actual forest area in ha (based on the NFI forest mask) under severe water stress.

Results showing which forest species were potentially affected by the drought of 2018 are displayed in Figure 11. *Fagus sylvatica* and *Fraxinus excelsior* were the two most frequent deciduous species that were potentially present in 90.2 and 81.4% respectively of severely water stressed forest areas. On the other hand, *Picea abies* and *Pinus sylvestris* were two most frequent needleleaf species potentially present in 46.4 and 40.6 % respectively of severely water stressed forest area across the extent of the study region.

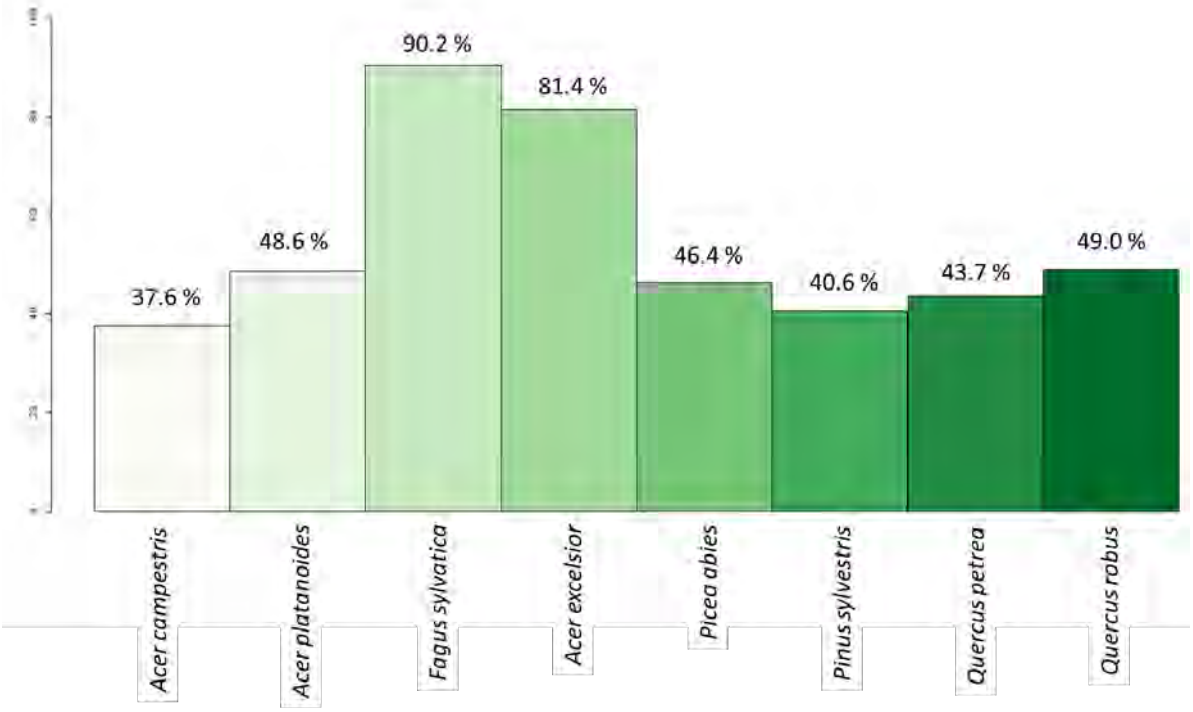

Figure 11: Percent of forest species potentially present at the areas under severe water stress in 2018.

Forest disturbances in 2019

Forest disturbances (tree-loggings/mortality) in 2019 detected using the method developed here are shown in Figure 12 for the extent of the study region. Looking at the map, we can observe a large number of disturbances in the regions around Walensee, central and northern Aargau, Solothurn and Basel. Another thing we can observe is the lack of disturbance data for the eastern part of the study region. In particular, approximately half of cantons St. Gallen and Appenzell Ausserrhoden are covered while no data exist for canton Appenzell Innerrhoden. This is due to the lack of cloud free Sentinel-2 data for the period April 15th to June 15th 2019 due to bad weather conditions and the orbital overlap of the sensor. As mentioned in the methods section, only areas with at least 3 Sentinel-2 observations were considered for further analyses. Since almost half of the area of cantons St. Gallen and Appenzell Ausserrhoden was available, we decided that this was a representative enough sample of the disturbances and included them in the results. Contrary, canton Appenzell Innerrhoden was excluded.

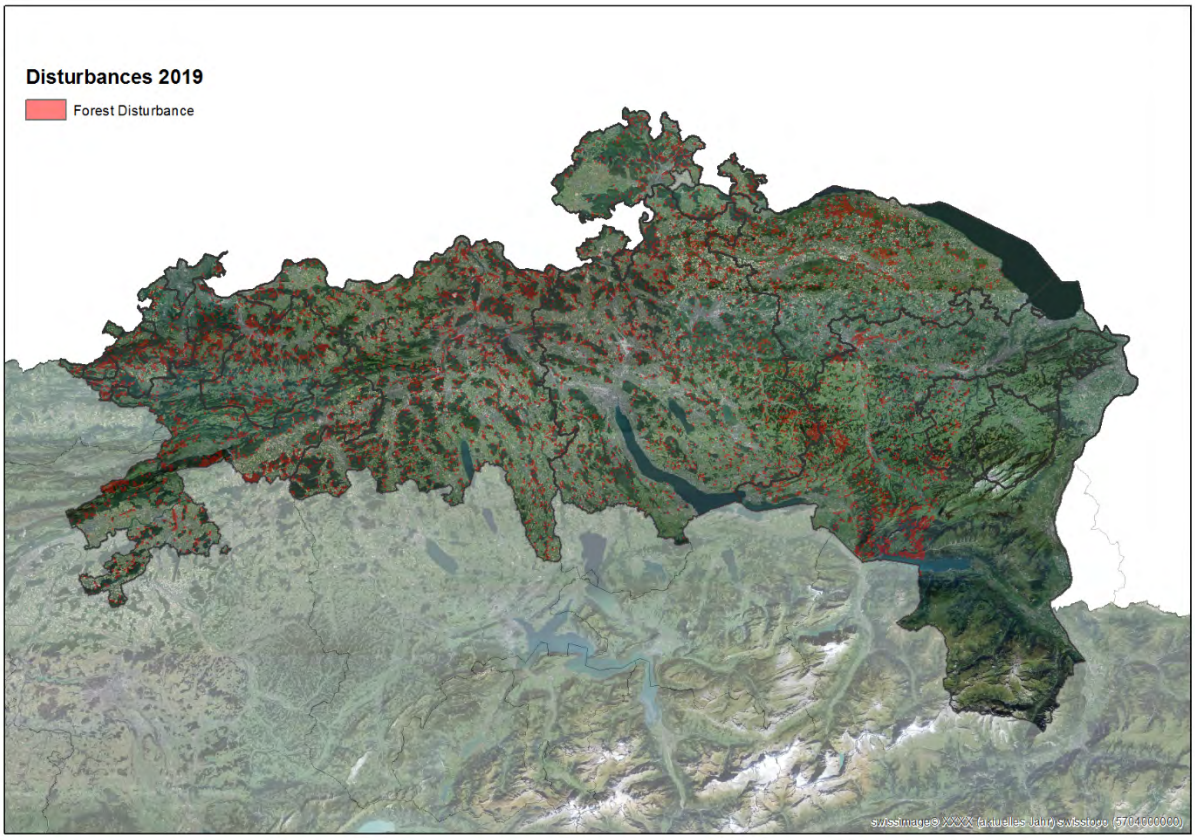

Figure 12: Forest disturbances in 2019 for the extent of the study region.

A total of 773 ha of forest disturbances were detected between the 2018 and 2019 that account for 0.33 % of the total forest in the study region. More detailed results at the level of different cantons are presented in Figure 13. We can see that while canton Aargau had the largest area of forest disturbances (146 ha) which accounted for 0.27% of the total forest area, contrary to canton Basel where we had detected smaller forest areas with disturbances (115 ha) but this accounted for 0.52% of the total forest area. Similar large areas of disturbances can be observed in cantons Solothurn and Thurgau (146 and 101 ha) that accounted for 0.41 and 0.45% of the total forest area. On the contrary, while large areas of disturbances were detected for canton Zurich (103 ha) these accounted for only 0.18% of the total forest area.

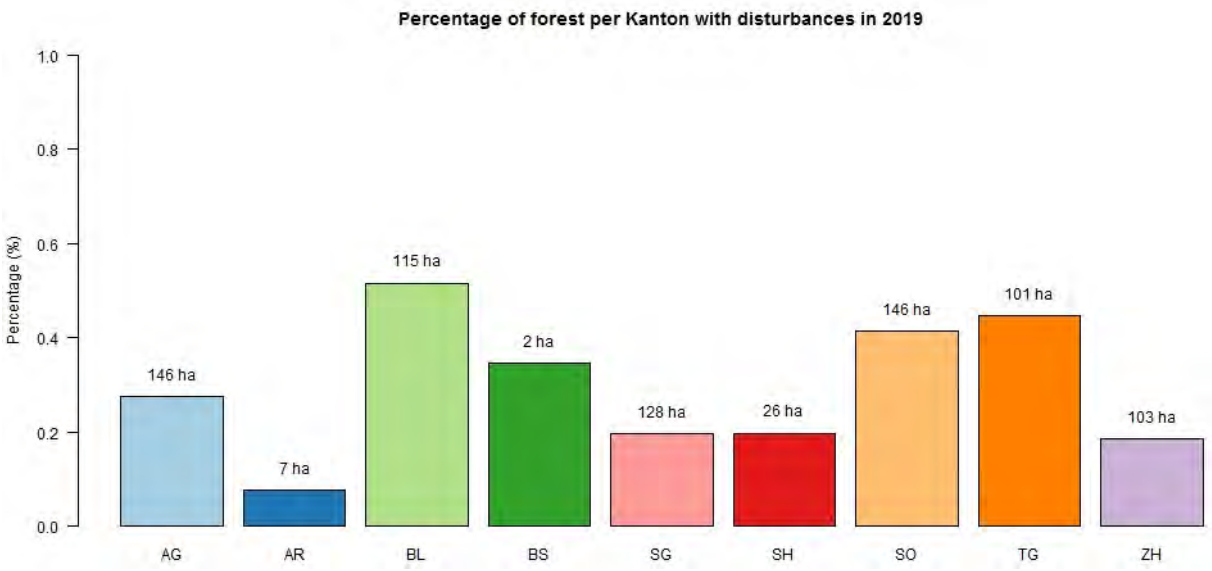

Figure 13: Percent of forest disturbances relative to the total forest area per canton within the study region. The numbers on top of the bars represent the actual forest area of disturbances in ha.

Link between drought stress in 2018 and disturbances in 2019

A final step of the analyses for this report was to see if there was a relationship between forest areas where disturbances were detected in 2019 and the drought stress (expressed as NDWI anomalies) of these areas in 2018. Results of these analyses are presented in Figure 14. We can observe that 75.1% of areas where disturbances were detected in 2019 had lower vegetation water content in 2018 compared to the period of normality defined as 2016-2017. Even if we consider the range of NDWI anomalies between -1 and + 1 SD as normal variation between years, 44.7% of disturbances in 2019 were detected in areas under moderate or severe water stress in 2018 contrary to just 5.7% of disturbances where vegetation water content was higher than normal in 2018.

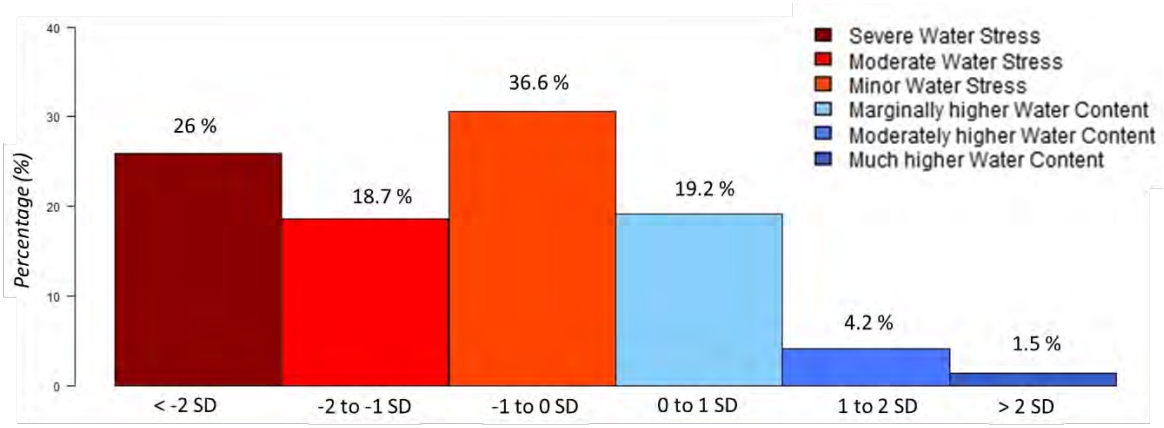

Figure 14: Relationship between forest areas where disturbances were detected in 2019 and their respective NDWI anomalies in 2018. For clarity, NDWI anomalies of 2018 are reclassified to four classes.

Discussion and conclusion

Overall, we conclude that using remote sensing data from the Sentinel-2 sensor has a large potential for mapping water stress but also for detecting large-scale disturbances of forest ecosystems in Switzerland. With the high frequency and rapid availability of Sentinel-2 data these results can be generated in near "real-time".

Using the NDWI anomalies of 2018 we were able to identify forest areas under moderate and severe water stress and quantify them at the level of cantons. While forest areas under severe water stress were overall proportional to the total forest area, variations between cantons still existed ranging from 10.4 to 17.4% of their total forest area.

Deciduous (*Fagus sylvatica)* and deciduous dominated forest (*Picea abies)* stands were primarily under severe water stress in 2018. As mentioned earlier in the report, even though species information was taken from potential distribution maps and not from maps of their actual distribution (which do not exist) these results provide a good initial basis for further analyses.

Using the method developed we were able to detect and map forest disturbances in 2019 using Sentinel-2 remote sensing data. Only large-scale disturbances like forest tree-logging and/or mortality of tree groups were however detected. This was because no actual fieldwork was done and ground truth was collected directly from high resolution remote sensing images. Regardless, we were able to identify cantons where larger disturbances took place and quantify the type of forest mixture and forest species that were affected the most.

Similar results to these of the forest drought stress were obtained with pure deciduous or deciduous dominated stands being tree-logging or where trees died. Interestingly, while *Fagus sylvatica* was the deciduous species which was more abundantly present in the 2019 disturbances, *Pinus sylvestris* was the most abundant needleleaf species. Linking the detected disturbances of 2019 to the water stress of 2018 we believe that there is a strong correlation between the two. While

some of the 2019 tree-logging can be attributed to normal or scheduled management practices a very large proportion of these areas was under severe water stress in 2018. This severe water stress caused by the drought potentially had direct effects on the tress (mortality) or made them vulnerable to bark beetle attacks, which eventually led to tree-logging. Regardless, field work is required to inspect the detected disturbances, discuss with forest practitioners and responsible authorities from different cantons before any final statements on the cause of the tree-logging or tree mortality can be made.

All analyses were performed using the distributed, cloud-based computing power of Google Earth Engine. Thus, there was neither need for downloading, storing and pre-processing of the remote sensing data nor the need for expensive hardware or cluster infrastructure. By using cloud processing, we were able to reduce processing times by orders of magnitude and could effortlessly adjust our analyses and study area.

Fungal infestation of *Pinus nigra* in Lower Austria with UAS

This study was conducted by Veronika Lechner, Marc Adams, Gerald Schnabel and Silvio Schüler at the Austrian Research Centre for Forests (BFW) (Lechner et al., 2019a & Ruhm et al., 2018).

Background

The natural spread-area of the black pine (*Pinus nigra Arnold*) in Europe stretches from eastern Spain over southern France, wide parts of middle and southern Italy, to the Balkans and far into western Turkey as well as to the islands Corsica, Sicily and Cyprus. In Turkey, the black pine has its largest occurrence at present with approx. 2.5 million hectares. Outside this closed distribution area in the Mediterranean region, there are natural black pine populations in Austria (Wienerwald), Romania and the Crimea. The Austrian black pine is thus the northernmost natural occurrence of this tree species. The pine forests in southern Lower Austria have dominated the landscape for many hundreds of years. In the Steinfeld, the region between Neunkirchen and Wiener Neustadt, as well as on the then bare mountains of the thermal line, Maria Theresia planted additional black pine trees to stop soil erosion and give people an economic basis. The black pine is therefore the character tree on the thermal line from the Schneeberg-Rax to the Vienna area. This character tree is currently massively affected by extreme climatic events and the interaction with a pest pathogen. Brown needles, dead shoots, branches and entire crowns in bright rust brown - the spread of a disease caused by a warmth-loving fungus is already visible in the Steinfeld area to the naked eye (Figure 15). The fungus (Diplodia sapinea) has been known in Austria since the 1960s and is known to have been causing severe damage since the 1990s. (Ruhm et al.,2018).

The extreme summer drought in 2015 resulted in favourable conditions for *Diplodia sapinea*, the Diplodia shoot dying pine. This led to major losses in stands dominated by black pine.. In some cases, the damage was so severe that it can be assumed that the plant's existence is threatened. The spread of the fungus is promoted by warm and humid weather in spring, followed by a very dry and hot summer. Within the possibilities of climate influence on the vitality of forests, the factor 'low precipitation' plays a primary role with regard to physiological stress. Although the core area of the infestation currently lies in the secondary black pine sites around Wiener Neustadt (Steinfeld, Größer Föhrenwald), it can be assumed that further warming and the more frequent occurrence of dry periods will also lead to a spread into primary black pine forests. This would have enormous consequences for the affected regions, considering the economic, ecological and cultural value of the black pine here (Ruhm et al.,2018).

Figure 15 Black pine stands near Steinfeld showing different degrees of Diplodia sapinea infestation.

80 - 90% of the Alpine east populations of the black pine are artificial. In the past, the use of resin played an important role. Today, the black pine along the thermal line is the only coniferous tree species that can be used in this climate. Furthermore, the black pine is a relict tree species on colline submontane pioneer sites. It is competitive on extreme sites on limestone and dolomite rootstocks, dry south-facing sites and initial rendzina. Its optimal growth is on deep, moderately fresh beech locations. As a pioneer tree species, the black pine is not very competitive with other tree species. Its occurrence is therefore limited to a few remaining locations of a formerly large area. It is a half-light tree species which tapers well under a light shade. Such a rejuvenation can, however, cause a problem due to the high fungal infestation by the infection of natural rejuvenation from infested old trees. The black pine is very resistant to storms (taproot system) even on very rocky soils. In addition, it is not sensitive to winter and late frost and is very resistant to dryness and drought (Ruhm et al.,2018).

UAS campaign

In an attempt to counter the spread of *Diplodia sapinea*, the BFW planned to establish a long-term monitoring at silvicultural level and implement operational adaptation measures to increase the resilience and maintain the vitality and biodiversity of yet uninfested black pine stands. Furthermore, a workflow based on the collection, processing and analysis of forest remote sensing data from different sources for the monitoring of infestation of black pine stands with *Diplodia sapinea* was developed

The following research questions were envisaged:

- Where are the hotspots located (e.g. within the stock or at the edge of the stock; predominantly in dense or in open stock)?
- Is (partially) automated detection and classification of damaged trees with (UAS-based) high-resolution orthophotos possible?
- Which of the parameters / indices derived from the images of the black pine stands represent the infestation with *Diplodia sapinea* in a statistically significant way? Is an upscaling by means of these indicators possible / reasonable?
- What is the temporal and spatial course of the disease? Are there hotspots? How do these hotspots develop in the course of the observation period?

To test the (technical) feasibility of employing UAS-photogrammetry in the context of these research questions and to make a first evaluation of the stages of infection, a 0.5 km² large stand of affected black pine was mapped in autumn 2016 near Steinfeld (Figure 16).

The aerial imagery was collected on 15 November 2016 between 09:00 AM and 01:00 PM with a Multiplex Mentor Elapor fixed-wing UAS (Figure 16, left). The original Mentor model was modified to add UAS capabilities: It was fitted with a GNSS sensor (3DR uBlox with LEA-6H compass kit) to determine its absolute position and an IMU (Inertial Measurement Unit) for orientation data; this data was managed by the on-board autopilot for autonomous flight (3DR ArduPilotMega) (Table 7, Appendix). An additional on-board GNSS unit (SM GPS-Logger 2) recorded 10 Hz positional data (x, y & z). After completing each flight, the GNSS data was synchronized with the recorded imagery (geotagging), to facilitate image-processing (Adams et al., 2016). The pre-flight mission planning to define flight path, height and speed was performed in the open-source software Mission Planner. Both flights were planned at 130 m a.s.l. with and overlap of 80 % along- and 80-95 % along-track overlap (Table 8, Appendix).

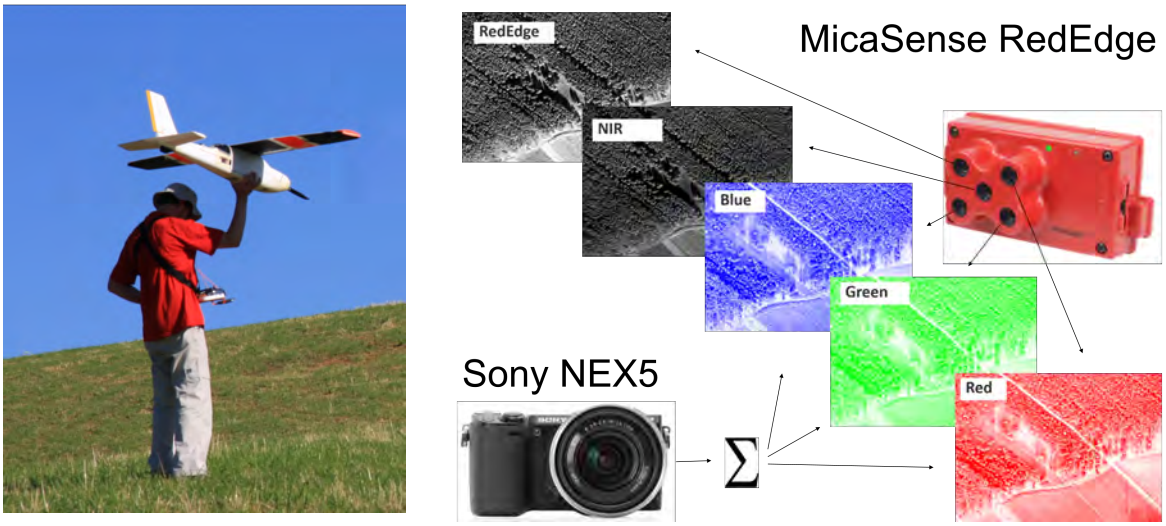

Figure 16 Multiplex Mentor UAS (left); daylight (Sony NEX5) and multispectral (Mica Sense RedEdge 3) cameras used on-board the Mentor, with corresponding spectral range (sources: MicaSense, dpreview.com, BFW).

Two different sensors were used to record imagery: i) a Sony NEX5 with 14MP sensor resolution fitted with a 16 mm prime lens to generate high-resolution RGB orthophotos (OP) and DSMs (0.05 m and 0.2 m, respectively); ii) a multispectral (MS) camera (MicaSense RedEdge 3), which consists of five synchronized cameras operating at different spectral ranges (Figure 16, right) with 5.5 mm prime lenses and 1.2 MP to calculate vegetation indices (0.1 m GSD). Both RGB and MS sensors were installed in the UAS fuselage to record 1,400 and 6,080 singles images, respectively. All basic camera settings were fixed pre-flight, as no telemetry was available (Table 8, Appendix); imagery was recorded with manual focus (Adams, et al., 2018).

Methods and Results

The UAS-images were processed with Agisoft Photoscan Pro (version 1.1.6) (Agisoft LLC, 2016), a commercially available photogrammetric software suite, that is widely spread in the UAS-community (Tonkin et al., 2014). It is based on a structure-from-motion algorithm and provides a complete, photogrammetric workflow, with particular emphasis on multi-view stereopsis (Harwin et al., 2015): i) tie point matching; ii) bundle adjustment (here constrained by assigning high weights to the GCP coordinates – known as indirect georeferencing or conventional aerotriangulation (Vander Jagt et al., 2015)); iii) linear 7-parameter conversion; removal of non-linear deformations; iv) dense point cloud (DPC) generation with multiview stereo reconstruction; v) export of georeferenced OPs and DSMs. We referenced all data to the respective standard national coordinate systems (EPSG-Code 31256, Gebrauchshöhen Adria). Figure 17 shows the resulting UAS-OP.

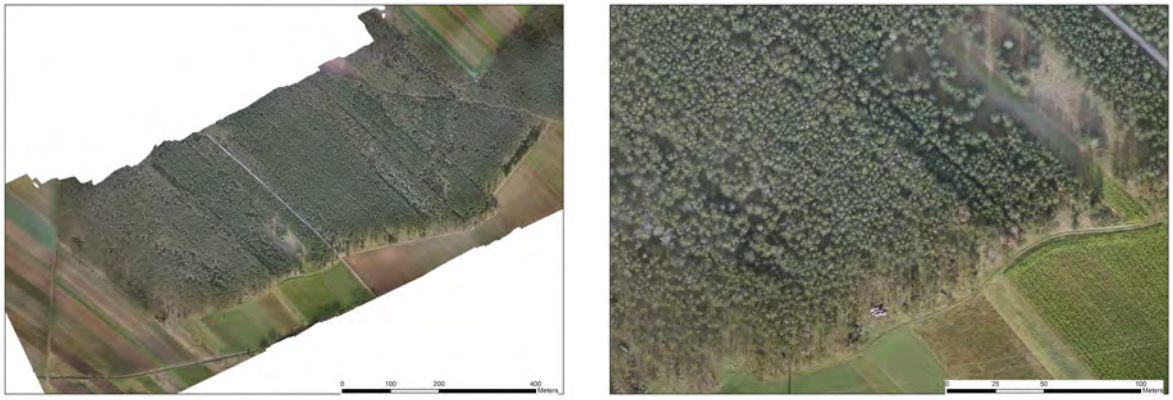

Figure 17 UAS-OP of the study site; overview (left) and detail (right).

Additionally, the normalized difference vegetation index (NDVI) was calculated based on the radiation in the Red and NIR channels of the MicaSense RedEdge multispectral imagery (Dimosthenis et al., 2019) and overlaid with the OP from the daylight camera (Figure 18).

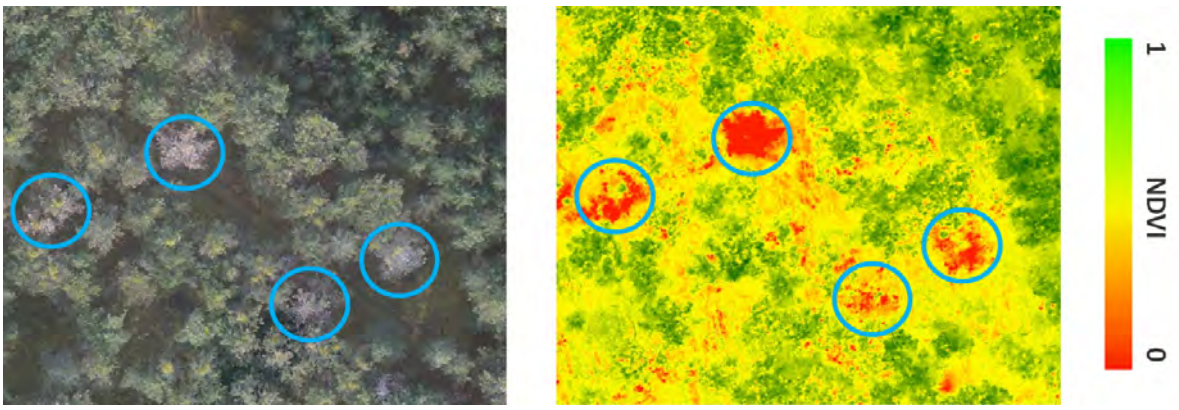

Figure 18 Comparison of RGB (left) and NDVI (right) imagery over infected Pinus nigra crowns (circled in blue).

The crowns of the black pines were manually delineated and assigned to three categories: healthy (1), infected (2) and dead (3). An NDVI-threshold was determined for each category. The comparison between the visual classification (RGB-OP) and the NDVI classification shows very good accordance for dead trees, sufficient for healthy and inconclusive for infected trees (*Figure 19* & *Figure 20*).

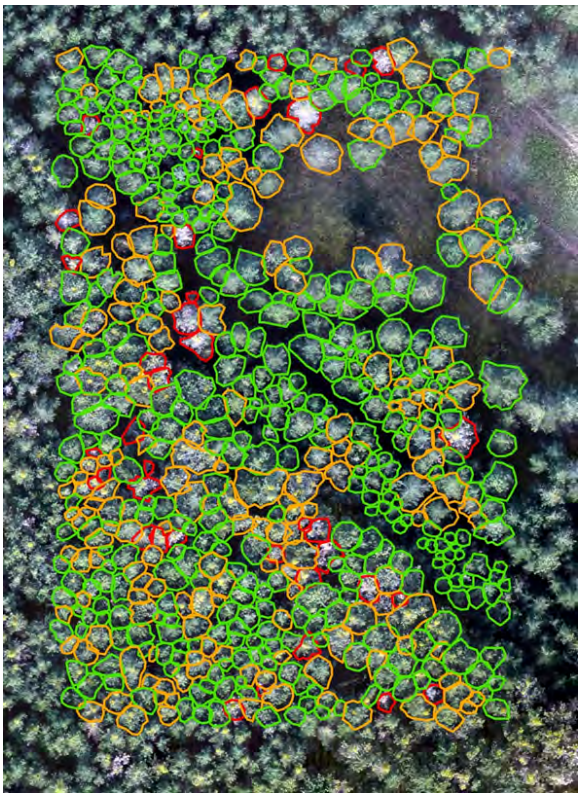

Figure 19 Subplot of Pinus nigra crowns classified into healthy (green), infected (orange) and dead (red) classes.

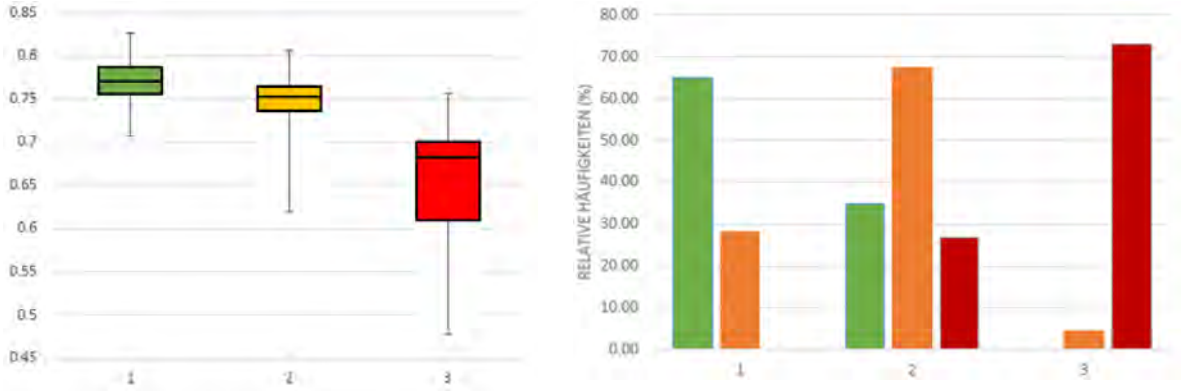

Figure 20 Distribution of NDVI-values within tree classes 1-3 (left) and relative frequency of trees classified as healthy, infected and dead within the same classes

In further investigations the automatic detection (NDVI threshold) is attempted to be improved to identify spreading patterns of the mycosis and support mitigation measures. Very detailed field surveys are planned to be undertaken to control the infection stage; in a next step these data will be compared with the UAS-P results (Lechner et al., 2019a).

Monitoring a forest fire area in Tyrol (UAS)

This study was conducted by Veronika Lechner, Alois Simon, Bernadette Sotier and Marc Adams in cooperation between the Austrian Research Centre for Forests (BFW), the Office of the Tyrolean Regional Government (AdTLR) and the University of Natural Resources and Applied Life Sciences (BOKU), with financing from the Flächenwirtschaftlichesprojekt (FWP) (Lechner et al., 2019b & Lechner et al., 2018).

Introduction

On 20 March 2014, a fire broke out below the Hochmahdkopf on the Absamer Vorberg (Tyrol, Austria), which spread quickly, favored by dried-out, dead grass vegetation and a foehn weather situation. The fire was caused by a thrown-away cigarette and burnt for several days before being extinguished by fire-fighters from air and ground. By the time the fire ended, also due to incipient snowfall on 23 March 2014, an area of around 70 ha had been burned, 54 ha of which were protection forest and mountain pine (Brenner et al., 2015) (Figure 21, left). In the area of the steep, south-facing slopes and rocky outcrops of the Hochmahdkopf, two fire events have already been documented in the 20th century. In 1923 an area of approx. 20-50 ha was affected (Grabherr, 1936) and in 1960 a small area of approx. 1.5 ha (BH Innsbruck Abt.II RegZ 99 SZ 1). Based on this, the 1980s saw an increased development of erosion channels, rockfall events and extensive soil erosion (Tiroler Landesforstdienst, 1985). The intensity of the erosion processes that occurred after these fire events is not documented in detail, but it was counteracted by afforestation and mitigation measures (Tiroler Landesforstdienst, 1985). Many of these measures were destroyed or severely damaged by the 2014 fire (Figure 21, right). Due to the substantial impact of the fire event on the area, an increased process activity regarding avalanches, erosion and rockfall was assumed. In addition, Sass et al. (2012) showed that long natural regeneration periods (50-500a) can be expected at sites in the Northern Calcareous Alps. Based on these assumptions, a land management project was developed (Tiroler Landesforstdienst, 2014). In addition to building avalanche defence structures (snow bridges and glide snow frames), reforestation measures were carried out and grass seed sown (Brenner, et al., 2015). The first afforestation were mainly carried out with the tree species white pine (*Pinus sylvestris*), spiral pine (*Pinus uncinata*), mountain maple (*Acer pseudoplatanus*), red beech (*Fagus sylvatica*) and mountain ash (*Sorbus aucuparia*). For grass seeding, a mixture of site-specific grasses (e.g. *Bromus erectus*, *Brachypodium pinnatum*, *Poa alpina*), herbs (e.g. *Clinopodium vulgare*, *Origanum vulgare*, *Teucrium chamaedrys*) and tree seeds (e.g. *Betula pendula*, *Pinus mugo*, *Pinus uncinata*, *Sorbus aria*, *Acer pseudoplatanus*) with 80% grasses and 20% herbs was chosen. This is intended to counteract erosion processes and promote natural regeneration.

Figure 21 Overview of lower burnt section at the Hochmahdkopf on 24 April 2014 (left); damaged avalanche defense structures and charred mountain pine in the upper burnt section on 10 April 2014 (right).

Shortly after the fire (BFW, 2014), as well as three years after the event (BFW, 2018), high-resolution aerial photographs were taken from low altitudes using various platforms and sensors, orthophotos and digital surface models (DSM) of the affected area were calculated. The objectives of these campaigns were: i) complete and timely documentation of the fire event; ii) monitoring the development of the area affected by the fire; iii) evaluation of the measures put in place. On the basis of these geodata, this case study deals with questions concerning the development of soil erosion and vegetation and discusses conclusions for monitoring forest fire areas with close-range sensing techniques.

Methods

A total of four campaigns were carried out after the event to collect aerial photographs of the burnt area: First, on 25 April 2014, a helicopter (type Lama) made a survey flight of the area of the study site and took first aerial pictures of the burnt area with a small format camera (Sony NEX5A, 14 MP). Based on this, the company Energie Burgenland GeoService was commissioned to conduct a systematic survey. This was carried out on 20 May 2014 by helicopter (type Ecureuil). A laser scanner (RIEGL LMS-Q560) and a medium format camera (ROLLEI AIC, 22 MP) were used. For accurate orientation of the aerial photographs, 10 photogrammetric measurement panels [0.4 x 0.4 m] were installed at defined points in the study area and surveyed with a terrestrial Global Navigation Satellite System (GNSS) (Trimble GeoExplorer XT 2008 Series). Three years later, on 10 May and 4 July 2017, a six-rotor multicopter twinHEX from twins.nrn Mechatronik was used for four flights. Data acquisition was performed with a multispectral camera (MicaSense RedEdge, 1.3 MP) and a small format camera (Sony QX1, 20MP). The aerial images were georeferenced using real-time kinematic GNSS on-board the copter. The platform-sensor combinations allowed a temporally and operationally flexible data acquisition of very high resolution aerial images (in the visual and

near infrared spectrum), as well as altitude information (laser scanner). Due to their low flight altitude of 150-300 m above sea level, these methods can be summarized under the term close-range sensing.

The processing of the overlapping aerial images was done in the photogrammetric software packages Agisoft Photoscan Pro and PIX4D Mapper. Orthophotos and DSMs with very high spatial resolution were calculated [0.03 - 0.1 m and 0.2 - 0.5 m Ground Sampling Distance (GSD), respectively]. Figure 22 shows an example of an orthophoto and a DSM from this geodata collection.

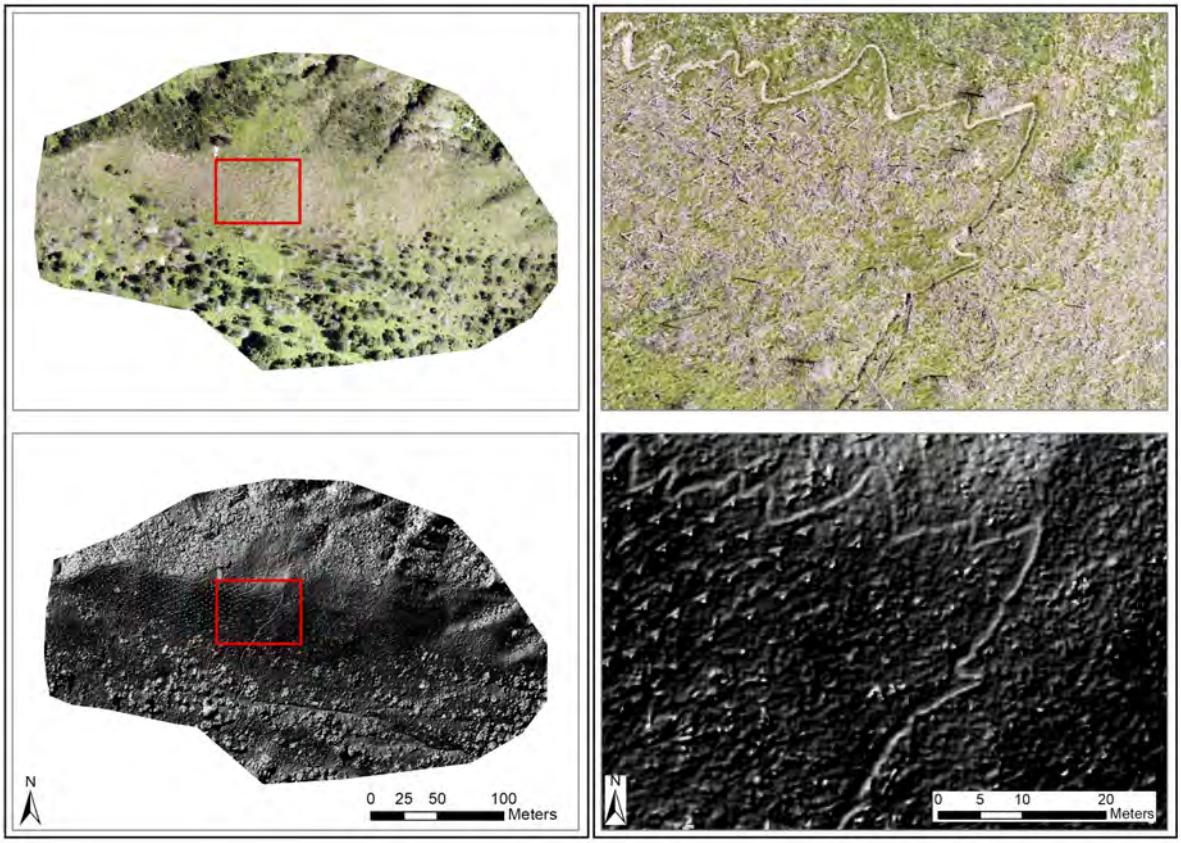

Figure 22 Results of the data collection on 4 July 2017 - orthophoto (top) in overview (left) and detail (right) (GSD: 0.05 m), Relief of the DSM (bottom) in overview (left) and detail (right) (GSD: 0.2 m); the red polygon indicates the enlarged area.

In order to evaluate the effectiveness of the measures taken after the fire (e.g. seeding, reforestation, avalanche defense structures, game management), detailed manual mapping of erosion intensity and vegetation was carried out on the basis of the orthophotos. Automated procedures (Wiegand et al., 2013; Mayr et al., 2016) show very good results for recording erosion areas from close-range sensing data. However, due to the small size of the area and the combined manual vegetation mapping with the orthophoto, the erosion intensity was also mapped manually.

In the course of the vegetation mapping, the following vegetation classes were distinguished: tree-/shrub-free zones (a - vegetation-free ground, b - sparse grass vegetation, c - extensive grass/herb vegetation) and tree-/shrub-covered areas (d - stand predominantly living, e - stand predominantly dead, f - mountain pine/shrub vegetation). The vegetation classes were compared with the vegetation mapping after the fire (BFW, 2014) in order to trace succession paths. The vegetation mapping was carried out for the entire mapped area.

To analyze the erosion development, two different approaches were followed: i) mapping from the orthophoto; ii) comparison of the DSMs. In addition, a 2015 terrestrial erosion mapping was available for evaluation (Hausberger 2016). However, this overlapped only partially with the flight area, so erosion mapping could only be carried out for approx. 60% of the total area. In the first approach, the erosion intensity was classified according to Hausberger (2016) as follows: low - share of eroded area < 25%, share of vegetation cover > 75%; medium - share of eroded area and vegetation cover 25-75%; high - share of eroded area > 75%, share of vegetation cover < 25%. The Hausberger terrain mapping (2016) was backed up with the current orthophotos and the polygon boundaries were adapted to the current state. The second approach tried to quantitatively substantiate this qualitative estimation of erosion intensities. For this purpose, the difference (ΔH) of the DSMs of 2014 and 2017 was calculated for the tree- and shrub-free areas as well as for the mapped vegetation classes

Results and discussion

The results of the vegetation development show that of the mountain pine areas affected by extensive full fire (vegetation completely burnt/charred) 20% have developed into class a) (vegetation-free soil), 60% into class b) (sparse grass vegetation) and 15% into class c) (extensive grass-weed vegetation). Tree stands were only selectively affected by fire, thus 65% fall into class d) (stand predominantly alive), 15% b), 10% c) and only 10% into class e) (stand predominantly dead). Crown fire (partially/completely scorched crowns) occurred much more frequently in the tree stands. About 35% of the areas affected by crown fires with high intensity are class e), about 45% were classified as living (class d). The area comparison of the erosion development showed a clear increase in areas with low erosion, while areas with high and medium erosion decreased strongly (Figure 23).

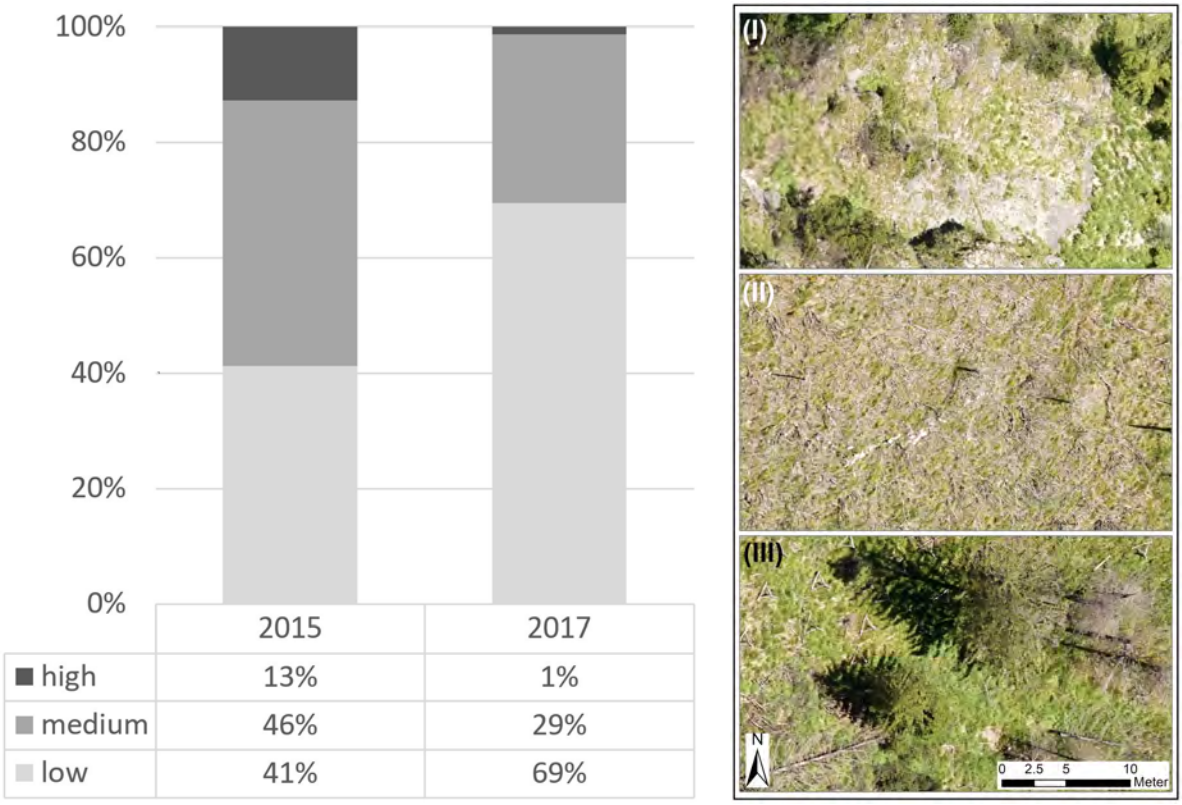

Figure 23 Comparison of the shares of the erosion classes in 2015 and 2017 (left); examples of the erosion classes based on the orthophoto 2017 (I - high, II - medium, III - low) (right).

The results of the erosion development confirm these results: Areas of higher erosion intensity also show a greater height difference than areas with low erosion intensity. When interpreting the erosion intensity, however, it should be noted that the range of variation is very high and that it is not the absolute values, but their relation to each other that is significant. For example, the denudation values recorded by Hausberger (2016) on a partial area and recorded over one year show a maximum mean erosion of 0.45 cm. However, a high dynamic of material erosion and accumulation was found. A comparison with literature values is difficult, as these refer mainly to mass balances per time unit (Shakesby & Doerr, 2006). If measured raw densities of the eroded material of 2.03 g/cm^3 (Absamer Vorberg, Hausberger, 2016) are used, this results in erosion values of approx. 6.7 mm per m^2/a (Sass et al., 2012) and 0.3 - 4.2 mm per m^2/a (Hausberger, 2016; depending on the calculation of the catchment area of the sediment traps) for comparable sites. For the considered period of three years, this results in values of 20.1 mm/m^2 and 0.97 - 12.6 mm/m^2, respectively (again depending on the calculation of the catchment area). If these values are compared with the analysis results in Figure 24, a deviation by a factor of 100 becomes

clear. Therefore, only the relative values of the erosion or vegetation classes should be compared. Here the vegetation class a) shows a 77 % higher erosion in the mean value compared to the vegetation class c). This also shows the importance of a rapid vegetation cover to prevent erosion, especially in vegetation-free areas. In order to detect erosion foci and to calculate soil erosion rates, they are too small-scale and too shallow in view of the height accuracy of the DSMs, as previous work has already shown (Leistner, 2011; Bremer & Sass, 2012). Statistically significant results could probably only be gained from an area of several m² with an average erosion depth of several decimetres.

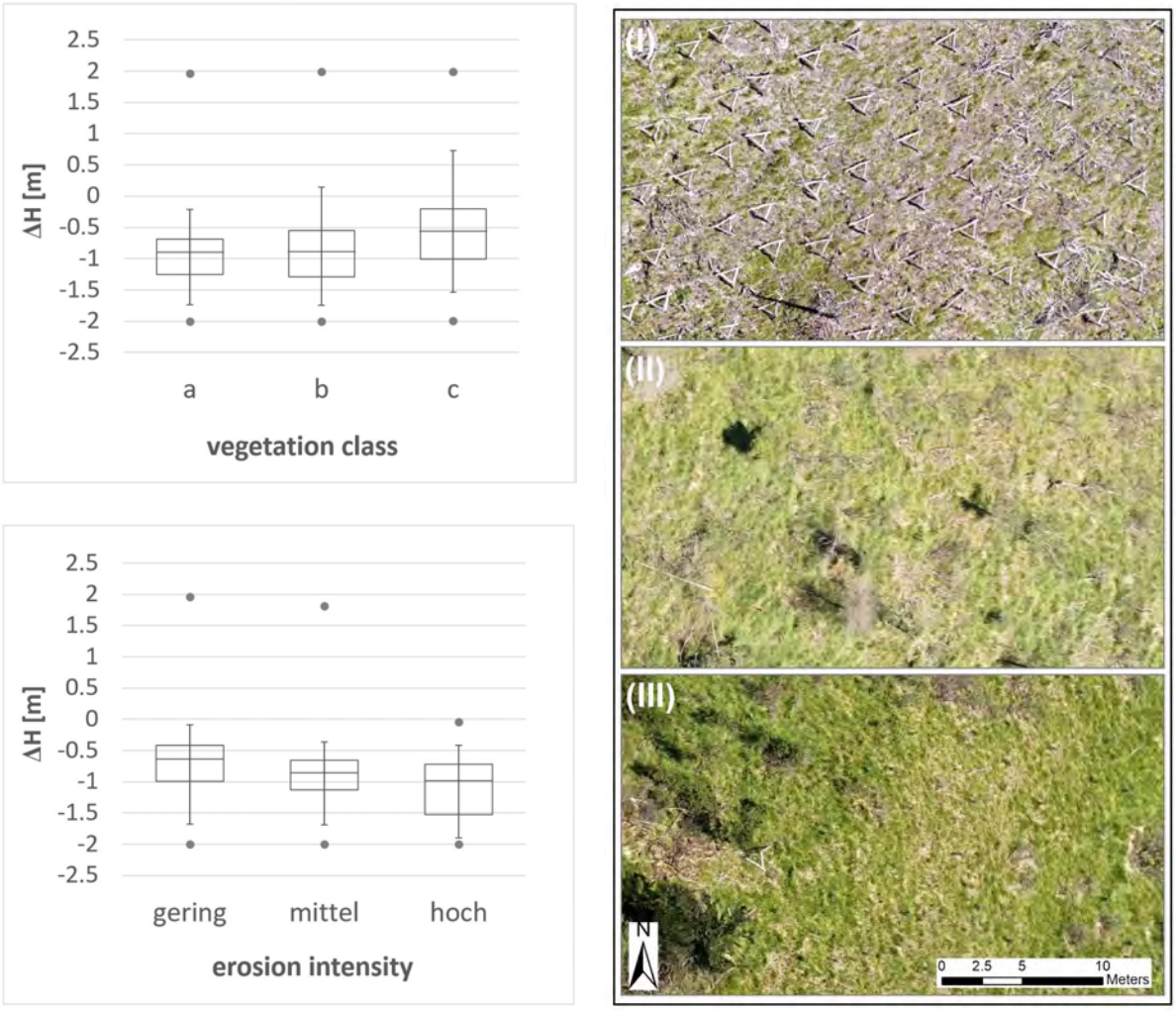

Figure 24 Height difference of the DSMs from 2014-2017 (left column) for the erosion intensities (top) and vegetation classes (bottom) (N = 12,891); examples of vegetation classes a) - vegetation-free soil (I), b) - sparse grass vegetation (II), c) - area-wide grass/herb vegetation (III) from the 2017 orthophoto (right column); the newly constructed glide snow frames are visible as triangular features in (I).

This analysis of the vegetation and erosion classes shows a favorable successional development of the examined area. Thus, a significant increase in the ground cover with grasses and herbs since the fire can be observed (Figure 25). A rapid regeneration of the ground vegetation was observed already one year after the event on areas with ground fire (Stubenböck, 2016). The increase in ground vegetation is associated with a stabilization and the decline of areas with high erosion intensity. This also applies to the mountain pine areas affected by full fire, which had a sparse ground vegetation and thus a low regeneration potential before the fire. The forest affected by crown fires shows a good resilience. In the areas affected by extensive crown fires (vegetation class e), no clear tendency is yet discernible, but here, too, initial stabilization by ground vegetation is likely. The post-fire mortality of trees, which occurred in the first year after the fire (Stubenböck, 2016), seems to have decreased significantly. In summary, it can be said that the goal of the short-term measures, i.e. the stabilization and reduction of the erosion intensity as quickly as possible, has been achieved. This is particularly important in mountain forests of the Alps, which show a low adaptation to fires compared to Mediterranean ecosystems. Thus, ecosystems frequently disturbed by fire show shorter regeneration periods (<10 a) of vegetation (Wittenberg et al., 2007) and a faster decrease of erosion rates (Cerdá & Lasanta, 2005). In contrast, fires in mountain forests of the Alps often lead to long regeneration periods (50-500 a) of vegetation (Sass et al., 2012), and to a long-term change in species composition (Moser et al., 2010) and thus to high erosion rates.

The effect of long-term measures for further regeneration of vegetation can only be assessed by continuous monitoring.

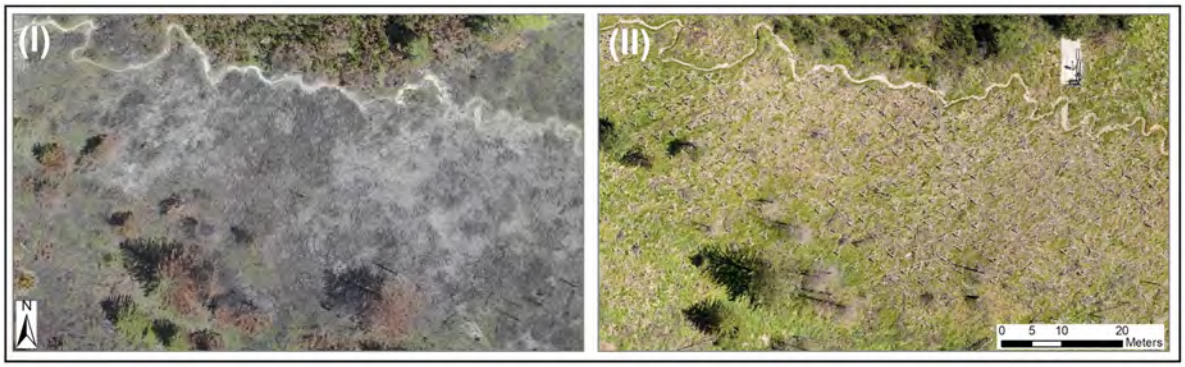

Figure 25 Detailed view of orthophotos from the lower burnt area of the Hochmahdkopf in 2014 (left) and 2017 (right), illustrating the rapid successional development in severely burnt areas.

Summary and outlook

The results have shown that close-range sensing methods are very well suited for monitoring forest fire areas. This is mainly due to the temporal and operational flexibility of the data collection on the tree- and shrub-free areas affected by the fire (vegetation mapping, height difference of the DSMs), and forest and shrub areas (vegetation mapping). A comparison of the used sensors shows that, due to the higher spatial resolution, the daylight camera is much better suited for vegetation mapping; the multispectral camera, on the other hand, allows data collection in the near-infrared range at lower spatial resolution and thus the calculation of vegetation indices. In the context of long-term monitoring, further multispectral mapping could serve to evaluate vegetation development by comparing the indices not only qualitatively but also quantitatively.

The generation of terrain models from photogrammetric data is associated with large uncertainties, especially for wooded areas and areas with low vegetation. The investigations have shown that a classification of the photogrammetric point cloud in the area of burnt vegetation (wooden skeleton) is only possible to a limited extent, because the wooden parts take up only a very small area and do not form a clearly distinguishable object. In the case of the Hochmahdkopf this was particularly noticeable in the area of the burnt mountain pines. Therefore, it is recommended to use only vegetation-free areas for the height comparison or to use other methods of data collection (e.g. multi-copter-supported laser scanning). It should be noted that the height accuracy decreases with the slope of the terrain, therefore erosion foci can only be detected from a few m^3 upwards. Shallow erosion areas can be mapped using high-resolution orthophotos. By comparing them with repeat photographs, the change in area of the erosions can be shown well.

It is recommended to choose the time of flight so that the grass is already green, so that the contrast to the bare ground is greater. In order to determine the vitality of the tree population, it should also have already sprouted. For the Hochmahdkopf a flight date in July proved to be suitable.

The appropriate time interval between flights depends on the processes to be observed. Traces of erosion can appear in the course of a few months / a season, the effect and development of afforestation measures and the recovery of the tree population can only be determined after several years. Since the highest erosion rates are expected in the years following a fire event (Sass et al., 2012) and further development is already apparent early on, shorter recording intervals (2-5a) in the first decade are reasonable. In the following periods, data collection in 5-10 year intervals may be sufficient. It is especially important to fly soon after the fire event to record the initial state.

Since the launch of the Sentinel missions of the European Space Agency (ESA) the availability of platforms, data hosts and processing platform services have skyrocketed. As end user, it is often difficult to keep an overview of the existing platforms and what the different platforms can offer. These often differ in data collections, different processing software and processing cloud services and processed products for specialists without remote sensing background.

In this chapter we try to give a rough overview of data hosts and processing platforms for three different types of end users in different tables.

1. Forest specialists who are looking for readily processed data sets for forest monitoring (Tables 3,4)

2. Natural hazard specialists who are looking for readily processed data sets for natural hazard monitoring (Table 3,5)

3. Remote sensing specialists who want to download satellite data themselves or process them on a processing server (Table 3,6)

The tables are non-exhausted as the market of data hubs and cloud processing services continuously develop at the moment. We will describe briefly some strength and challenges with the different solutions given in the tables.

Advantages and disadvantages of the different sensors

For the detection and recording of changes in forests, passive sensors and active sensors have both advantages and disadvantages.

Passive multispectral sensors such as Sentinel-2 or Landsat have the advantage that their data can be interpreted very intuitively. Representations of the blue-green-red channels, the RGB representation corresponds to what we are used to with our eyes. The images are easy to interpret. In times of Google Maps and Bing Maps, orthoimages and satellite maps in the RGB representation are commonplace and do not need any additional explanation. Dead trees and damage after storms or fire can be recognized very intuitively.

For finer differentiation, the multispectral data can be used to easily create false-color infrared images (Table 3, Data access hubs). Experts in the forest remote sensing sector have been familiar with these CIR data for a long time. Damage to trees and loss of vitality can be detected even better with the information from the red spectrum and the near infrared than with the information from the RGB (Tables 3, 4)

The major disadvantage of passive multispectral sensors is that clouds prevent visibility of the earth's surface. Therefore, when clouds are overcast, no data can be recorded below the clouds. This limits the availability of data very much. The temporal resolution of five days for Sentinel-2 and

16 days for Landsat is thus put into perspective. It can happen that, for example, after a storm event, several weeks can pass before cloudless conditions prevail during a satellite overflight.

This is where the strength of the active sensors, such as Sentinel-1 (synthetic aperture radar – SAR), comes into play. The active sensor penetrates an existing cloud cover and records information from the earth's surface. However, the interpretation of the backscatter is more difficult than with passive multispectral data and needs expert knowledge, though several data hubs offer now special preprocessed data that are more readily available (Tables 3,4 6). Temperature, vegetation and soil moisture have a large influence on the backscatter and can make the quantification of changes in forests difficult.

When selecting sensors and platforms, it is therefore always important how quickly and how detailed information is required. If I need to obtain information about large areas very quickly in order to plan resources for e.g. damage management, I will use radar data in bad weather to obtain indications of damage. If there are cloudless conditions, the sensor of choice is certainly multispectral Sentinel-2 data that is easy to interpret and analyze.

For local, small-scale events (e.g. landslides or local bark beetle calamities) UAS systems are already very easy and fast to use today. Legal requirements must be met, but in this way, data can be collected very quickly for the localization of damages.

Table 3 gives a non exhausted overview of data access hubs for various satellite missions. Downloadable products might be of interest for foresters, remote sensing specialists and natural hazard specialists. Optical products are easy accessible and self-explained such as on Sentinel Hub, Sentinel Playground, ESA Forest Monitoring Services and Google Earth Engine. Other data hubs offer cloud processing services, additional data set and specialist software (Copernicus ONDA, CREODIAS, EODC, JRC Earth Observation Data and Processing Platform, Forestry Thematic Exploitation Platform, SwissDataCube).

Table 3 Data hubs to access satellite imagery for various applications, including some data hubs with excessive cloud processing services, additional data sets and specialist software

Data hub	Access	Terms and conditions	Application
ASF Vertex	MODIS/Terra Vegetation Indices, Sentinel-1, ERS, RADARSAT-1, ALOS-PALSAR	open access	NDVI and Enhanced Vegetation Index (EVI)
ESA Forest Monitoring Services	Sentinel-1,Sentinel-2, Pleiades, CryoSAt, ALOS, ENVISAT, ERS,	PI proposal	Forest monitoring
Forestry Thematic Exploitation Platform	Sentinel-1, Sentinel-2, Landsat-5/7/8, ERS1/2, Envisat ASAR, DEM, ALOS PALSAR, JERS, Pleiades, Spot, SAOCOM, RapidEye	PI Proposal	Access to EO data, efficient data exploitation, various GIS and EO toolboxes, user interface for basic processing tasks, vegetation idices, forest changes, land cover, biomass
Copernicus Open Acess Hub	Sentinel-1, Sentinel-2, Sentinel-3, Sentinel-5P	One-time registration	Large choice of different services - under continuous change

Copernicus ONDA	Sentinel-1, Sentinel-2, Sentinel-3, Sentinel-5P	costs	Data access, data storage cloud services, virtual servers, managed services, processing tools (SNAO, Sen2Cor, Snaphu)
Copernicus sobloo	Sentinel-1, Sentinel-2, Sentinel-3, Sentinel-5P	costs	Data access, data storage, cloud services, virtual servers, managed services, processing tools (SNAO, Sen2Cor, Snaphu)
Copernicus CREODIAS	Sentinel-1, Sentinel-2, Sentinel-3, Sentinel-5P, Landsat-5,7,8, Envisat, SMOS	annual costs	Cloud dashboard, Jupyter notebook
EODC	Sentinel-1, Sentinel-2, Sentinel-3	annual costs	Cloud processing data access and storage, Jupyter notebook, Austrian data sets (restricted at the moment), QGIS remote desktop
Sentinel Hub	Sentinel-1, Sentinel-2, Sentinel-3, Sentinel-5P, Landsat 5,7,8,8, Envisat Meris, Proba-V MODIS, GIBS	monthly costs	Cloud processing and storage
JRC Earth Observation Data and Processing Platform	not online yet	not online	Jupyter notebooks, QGIS remote desktop, HTCondor, storage and processing infrastructure
Sentinel Playground	Sentinel-2: SWIR, NDWI	just visualization	Download of image files
Google Earth Engine	Sentinel-1, Sentinel-2, Landsat, MODIS, Surface temperature, Climate, Atmosphere, Weatther, Geophysical data, Landcover data, Cropland data	no download of data but cloud-based analysis platform	MODIS Leaf Area Index, satellite imagery catalog, analysis capacity,
Planet	RapidEye, PlanetScope, SkySat	costs	Cloud analysis, fully-automated imagery processing, for forestry: sub-1m multispectral Skysat imagery, geospatial analysis service for desease analysis Czech Republic
Digital Globe	WorldView-4, WorldView-3, WorldView-2, WorldView-1, GeoEye-1, QuickBird, IKONOS	costs	Critical infrastructure monitoring, short-wave infrared (SWIR) at 3.7 m, fire detection, soi moisture content, etc.
Geoland	Forestry maps and forest management plans from some countries	open access	Geodata Austria
CEOS -COVE	All satellites		Potential future satellite coverage tool, satellite acquisition forecaster
DLR	TerraSAR-X, Tandem-X	PI proposal for research only	SAR applications
TerraSar-X | TANDEM-X	Spot, TerraSAR-X, Pleiades	Costs	Download, no services
Deimos Imaging	Deimos-1, Deimos-2	Costs	
NASA Langley Atmospheric Science Data Center	Vegetation Earth System Data Record (VESDR)		Leaf Area Index (LAI), diurnal courses of NDVI, Sunlit Leaf Area (SLA), fraction of incident photosynthetically active radiation (400-700 nm) absorbed by the vegetation (FPAR) and directional area scattering function (DASF)

SwissDataCube	Landsat 5/7/8 1984-2017, Sentinel-2 (2015-2018), Swiss geodata	Archive Landsat 1983-2017, Sentinel-1, 2	EO monitoring tool , open data cube open-source analytical framework
NASA Multi-Mission Algorithm and Analysis Platform	BIOMASS, GEDI, NISAR	One-time NASA registration	Exploitation of earth observation (EO) data of the BIOMASS, GEDI, and NISAR missions, data, computing capabilities, tools, algorithms

For forest monitoring Table 4 gives a non exhausted overview of ready to use data sets and maps, readily available for forest specialists. Several products on tree cover density, forest type and dominant leaf types are available, such as from the Copernicus HR Forest service and on Earth engine (Global forest change 2000-2018) (Hansen et al. 2013). Though, the update of these maps is not available annually and the resolution might not be high enough for regional forest management, the maps still offer an invaluable asset as base for regional studies. A processing chain using grayscale and color display of SAR imagery has been developed to provide time series of forest degradation and deforestation and needs rather remote sensing specialist knowledge (Kellndorfer 2019).

Table 4 Overview of forest monitoring products such as global forest change, dominant leaf type, tree cover density forest type,, storm damages and drought effects

Product	Platform / mission	Method	Reference	Data access hubs
Tree cover gain and loss (2001-2012), tree cover canopy density	Landsat	30x30 m, 2001-2012, tree cover canopy density, Landsat data, Google Earth Engine & algorithms	Hansen et al. 2013	Global Forest Watch
Tree cover density change (2012-2015)	Sentinel-2, Landsat	level of tree cover density in a range from 0-100%, 2012-2015, status maps and change maps	EEA 2017	Copernicus HR Forest Layer
Dominant leaf type (2015)	Sentinel-2, Landsat	Dominant leaf type providing information on the dominant leaf type: broadleaved or coniferous	EEA 2017	Copernicus HR Forest Layer
Forest type (2015)	Sentinel-2, Landsat	1) a dominant leaf type product that has a MMU of 0.5 ha, as well as a 10% tree cover density threshold applied, and 2) a support layer that maps, based on the dominant leaf type product, trees under agricultural use and in urban context	EEA 2017	Copernicus HR Forest Layer
Tree cover loss/gain (2001-2001-2018), tree cover canopy density	Landsat 7 and 8	30x30 M 2001-2018, Google Earth Engine & algorithms	Hansen et al. 2013	Global Forest Watch
Storm damage	Sentinel-1	SAR David Small UZH, Small et al., 2019	Rüetschi et al. 2019	Online Map Wind Damage

World fire atlas	Sentinel-3	ONDA platform using ESA Snap and GDAL tools		Sentinel-3 World Fires Atlas Prototype
OGVI (OLCI Global Vegetation Index): fraction of absorbed photosynthetically active radiation (FAPAR) in the plant canopy.	Sentinel-3	Visualization of level3 geophysical quantities with monthly acquisition, processed by missions ground segments	https://worldwind.earth/	Earth Starts Beating
OTCI (OLCI Terrestrial Chlorophyll Index): it estimates the chlorophyll content in terrestrial vegetation and aims at monitoring vegetation condition and health.	Sentinel-3	Visualization of level3 geophysical quantities with monthly acquisition, processed by missions ground segments	**https://worldwind.earth/**	Earth Starts Beating
CHL: Chlorophyll-a concentration, computed using OC4Me algorithms. Measured in mg*m-3	Sentinel-3	Visualization of level3 geophysical quantities with monthly acquisition, processed by missions ground segments	https://worldwind.earth/	Earth Starts Beating
Leaf Area Index / 4-day global 500 m pixel	MODIS	The MCD15A3H V6 level 4, Combined Fraction of Photosynthetically Active Radiation (FPAR), and Leaf Area Index (LAI) product is a 4-day composite data set with 500 meter pixel size.	GEE Forest	https://developers.google.com/earth-engine/datasets/catalog/MODIS_006_MCD15A3H
Drought effects Forest species	Sentinel-2	Normalized Different Water Index (NDWI) = normalized difference between the Near-Infrared (NIR) and Short Wave Infrared (SWIR) channels of the electromagnetic spectrum	Psomas et al. 2019, this report	-
Global forest change 2000-2018	Landsat bands 3,4,5,7	Time-series analysis of Landsat images in characterizing global forest extent and change.	https://developers.google.com/earth-engine/datasets/catalog/UMD_hansen_global_forest_change_2018_v1_6	http://earthenginepartners.appspot.com/science-2013-global-forest

Table 5 Overview of selected satellite products with a variety of processing levels that are useful for the exploration of natural hazards such as snow cover and landslides

Product	Platform / Mission	Method	Processing level	Reference	Data access Hubs
Snow masks	Sentinel-2	MUSCATE	Level2B		Copernicus sobloo
Surface changes by Sentinel-1	Sentinel-1	HARRIS SARscape	Prototype	https://www.onda-dias.eu/cms/marketplace/demystifying-sar-data-processing/	Harris GSF Dashboard ONDA
Surface Deformation Service	Sentinel-1 and CosmoSky Med	SBAS-InSAR	Available for a pilot region	IREA	Copernicus ONDA
Several processing cloud services to explore geohazards such as slope deformations, volcanic and earthquake activity	Sentinel-1, Sentinel-2, Sentinel-3, Sentinel-5, ENVISAT, ERS, etc. for thematic exploitation	Data access, processing facilities, platform as a service, Adore Doris interferometric processor, Coin, COMBI Band, DIAPASON InSAR, DSM-OPT, Fastvel processing service (PSI-based mean displacement velocity maps), Gamma DInSAR, Gamma5sar, MPIC-OPT, PF-ERS, PSI post-proc, SBAS-Stripmap, SNAC, StaMPS, Sentinel-1 Medium-Resolution InSAR Browse Service	Proposal-based research access		Geohazards Thematic Exploitation Platform and Portal
European Ground Motion Service (planned for 2021)	Sentinel-1, update annually	100x100 m	Level 2a, Level2b, Level3	Larsen et al. 2019	European Ground Motion Service
Terra Snow Cover Daily Global 500 m	MODIS	The MOD10A1 V6 Snow Cover Daily Global 500m product contains snow cover, snow albedo, fractional snow cover, and quality assessment (QA) data. Snow cover data are based on a snow mapping algorithm that employs a Normalized Difference Snow Index (NDSI) and other criteria tests.	Level3	https://nsidc.org/data/mod10a1	https://developers.google.com/earth-engine/datasets/catalog/MODIS_006_MOD10A1
Global Precipitation (rain and snow) Measurement near-real-time every 3 hours	Multi-satellite retrievals	passive-microwave instruments	research level products	https://www.nasa.gov/mission_pages/GPM/overview/index.html	https://developers.google.com/earth-engine/datasets/catalog/NASA_GPM_L3_IMERG_V06

Table 5 gives some examples specialized products to monitor and research gravitational mass movements. The chosen examples are useful for avalanche research in terms of ready to use products such as the global precipitation or daily snow cover services. The European Ground Monitoring Service is planned to be online in 2021 and will be a benchmark for the monitoring of slope deformations (mm/yr). Slope deformations often host secondary processes as soil and rock slope failures as described in chapter 4 in D.T.1.3.2 .

Table 6 summarizes some of the most useful satellite platforms with passive and active sensors such as Landsat, Sentinel-1/-2, Envisat, TerraSAR-X. The summary gives an overview of which bands and wavelengths the different sensors cover, the repeat cycle of the satellite platforms and if data are accessible on an open access policy or if the user needs to consider costs to use these data.

Table 6 Satellite data access points for remote sensing specialists

Satellite system	Mission Start/ Complete	Band / Wavelength	Repeat Cycle	Spatial Resolution	Application	Data Hub	Alternative Data Hub
Landsat 7	1999 - *	0.52 – 0.90 µm 0.45 – 0.52 µm 0.53 – 0.61 µm 0.63 – 0.69 µm 0.78 – 0.90 µm 1.55 – 1.75 µm 2.09 – 2.35 µm	16 days	PAN: 15m Others: 30m	Forestry monitoring, geologic mapping, natural hazard mapping	Google Earth Engine	CREODIAS
Landsat 8	2013 - *	0.50 – 0.68 µm 0.43 – 0.45 µm 0.45 – 0.51 µm 0.53 – 0.60 µm 0.63 – 0.68 µm 0. 84 – 0.88 µm 1.36 – 1.39 µm 1.56 – 1.66 µm 2.10 – 2.30 µm	16 days	PAN: 15m	Forestry monitoring, geologic mapping, natural hazard mapping	Google Earth Engine	CREODIAS
Sentinel-1	2014 -	C-band, 5.6 cm	6 days		Forest mapping, surface displacement maps, snow cover	Copernicus SciHub	CREODIAS
Sentinel-2	2015 2017 (~ 2027)	0.44 +/- 0.02 µm 0.4 +/- 0.065 µm 0.56 +/- 0.04 µm 0.67 +/- 0.03 µm 0.71 +/- 0.02 µm 0.74 +/- 0.02 µm 0.78 +/- 0.02 µm 0.84 +/- 0.12 µm 0.87 +/- 0.02 µm 0.95 +/- 0.02 µm 1.38 +/- 0.03 µm 1.61 +/- 0.09 µm 2.19 +/- 0.18 µm	10 days (Sentinel-2A); 5 days (Sentinel-2A & 2B)	B2,B3,B4, B8: 10m B5,B6,B7, B8a,B11,B12: 20m B1,B9,B10 : 60m	Forestry monitoring, plant indices, leaf area chlorophyll	Copernicus SciHub	CREODIAS

Sentinel-3AB	16.02.2016 25.04.2018	Temperature		300 m	Bigger picture monitoring forest, wildfires, vegetation state	Copernicus SciHub	CREODIAS
ERS 1	1991-2001	C-band, 5.6 cm, 4-8 GHz	35 days	30 m	Slope deformations, ground motion	Copernicus SciHub	
ERS 2	1995-2011	C-band, 5.6 cm, 4-8 GHz	35 days	30 m	Slope deformations, ground motion	Copernicus SciHub	
Envisat	2002-2012	C-band, 5.6 cm, 4-8 GHz	35 days	28 m	Slope deformations, ground motion	Copernicus SciHub	CREODIAS
MODIS/Terra	2001-	Normalized Difference Vegetation Index (NDVI), Enhanced Vegetation Index (EVI)	16 days	1 km	Vegetation Indices, improved sensitiviy over high biomass regions	LPDAAC USGS	USGS
CosmoSkyMed	2007-	SAR X-band		Spot: 1m; Stripmap: 3-5 m; ScanSAR: 30-100 m	Slope deformations, ground motion, forest monitoring	e-GEOS	
ALOS-1 PALSAR	2006-2011	L-band; 24.6 cm	46 days	Spot: 1-3 m, Stripmap: 3-10 m; ScanSAR: 25-100 m	Slope deformations, ground motion, forest monitoring	Limited proposal-based scientific	Commercial
Pleiades HiRi	2011-	Panchromatic at 0.5 m, pansharped colour image at 0.5 m, multispectral image in 4 spectral bands at 2m	daily revisit capacity	50 m	Landslide detection, forest monitoring	Airbus - Pleiades	Commercial
TerraSAR-X	2007-	X-band; 3 cm wavelength (9.65 GHz frequency)	11 days	Spot: 0.2x3.5 m; Stripmap: 3x3 m; ScanSAR: 18-40 m	Slope deformations, ground motion, forest monitoring	DLR research, restrained scientific (always lowest priority)	Commercial

Appendix

Table 7: Technical specifications of the Mentor UAS (Adams et al., 2016)

UAS type	Fixed-wing (custom-built)
Dimensions	1.6 m (wing span); 1.2 m (fuselage)
Engine	1 electrical, brushless motor
Flight time	30–40 minutes
Max. range / coverage	1,500 m / 0.6 km²
Empty weight	2.3 kg
Max. take-off weight	2.8 kg
Max. payload weight	0.5 kg
Navigation	3DR APM 2.6 (IMU, barometer) 3DR uBlox GNSS with Compass Kit uBlox LEA-6H module
Wireless communication	Graupner MX-20 HOTT 2,4 GHz (sender) Frequency 2,400 … 2,484.5 MHz Graupner GR-16 HOTT 2.4 GHz (receiver)
LiPo battery	LiPolice GreenLine Light Edition 5s 4,900 mAh (0.6 kg)

Table 8: Properties of UAS-flights on 15 November 2015.

Sensor	Sony NEX5	Mica Sense Red Edge
Overlap (along- / cross-track)	80 / 80%	80 / 95%
Flight height	130 m a.g.l.	130 m a.g.l.
Flight speed	12–14 m s^{-1}	12–14 m s^{-1}
Image format	JPEG (high quality)	TIF (12-bit)
Exposure (fixed)	1/320–1/800	1/400–1/1000
ISO (automatic)	100–400	200-800
Aperture (automatic)	f/2.5–18	f/2.8

References

Adams, M.S., Bühler, Y. & Fromm, R. 2018. Multitemporal accuracy and precision assessment of unmanned aerial system photogrammetry for slope-scale snow depth maps in alpine terrain. Pure and Applied Geophysics 175, 9, 3303–3324.

Adams, M.S., Fromm, R. & Lechner, V. 2016. High-Resolution Debris Flow Volume Mapping with Unmanned Aerial Systems (UAS) and Photogrammetric Techniques. The International Archives of the Photogrammetry, Remote Sensing and Spatial Information Sciences, Volume XLI-B1, XXIII ISPRS Congress, 12–19 July 2016, Prague, Czech Republic.

AgiSoft LLC, 2016. Agisoft PhotoScan, professional edition, version 1.1.6 64 bit, Petersburg, Russia.

Ambrosia, V., Wegener, S., Zajkowski, T., Sullivan, D., Buechel, S., Enomoto, F., Lobitz, B., Johan, S., Brass, J. & Hinkley, E. 2011. The Ikhana unmanned airborne system (UAS) western states fire imaging missions: from concept to reality (2006–2010). Geocarto International 26(2): 85–101.

Banskota, A., Kayastha, N., Falkowski, M.J., Wulder, M.A., Froese, R.E., White, J.C., 2014. Forest monitoring using Landsat time series data: a review. Canadian Journal of Remote Sensing, 40(5), 362-384.

Baumann, M., Ozdogan, M., Wolter, P.T., Krylov, A., Vladimirova, N., Radeloff, V.C., 2014. Landsat remote sensing of forest windfall disturbance. Remote Sens. Environ. 143, 171–179. https://doi.org/10.1016/j.rse.2013.12.020

BFW 2014. Technical Report Flight Campaign and Analysis [Technischer Bericht Befliegung und Auswertung] Absamer Vorberg (Hochmahdkopf) 2014. Austrian Research Centre for Forests (BFW), Innsbruck, (not published).

BFW 2018. Technical Report Flight Campaign and Analysis [Technischer Bericht Befliegung und Auswertung] Absamer Vorberg (Hochmahdkopf) 2017. Austrian Research Centre for Forests (BFW), Innsbruck, (not published).

Bremer, M. & Sass, O. 2012. Combining airborne and terrestrial laser scanning for quantifying erosion and deposition by a debris flow event. Geomorphology 138, 49-60.

Brenner, G., Raggl, P., Schreiner, I. & Simon, A. 2015, Forest Fire on Vorberg Mountain near Absam (Tyrol) [Der Waldbrand am Absamer Vorberg (Tirol)]. Journal of Torrent, Avalanche, Landslide amd Rock Fall Engineering, 175, 79.

Briese, C., Fortner, R., Sager, P. &Pfeifer, N. 2013. Vom Modellflughobby zu unbemannten Flugsystemen für die Geodatenerfassung. Österreichische Zeitschrift für Vermessung und Geoinformation (VGI), 101, 2+3, 64-74.

Broge, N. H., and E. Leblanc. 2001. Comparing prediction power and stability of broadband and hyperspectral vegetation indices for estimation of green leaf area index and canopy chlorophyll density. Remote Sensing of Environment 76:156-172.

Brun, P., A. Psomas, C. Ginzler, W. Thuiller, M. Zappa, and N. E. Zimmermann. 2020. Large-scale premature wilting in Central European forests during the 2018 summer drought. In Prep.

Brunner, M. I., K. Liechti, and M. Zappa. 2019. Extremeness of recent drought events in Switzerland: dependence on variable and return period choice. Nat. Hazards Earth Syst. Sci. 19:2311-2323.

Bühler, Y., Adams, M.S., Boesch, R. & Stoffel, A. 2016. Mapping snow depth in alpine terrain with unmanned aerial systems (UAS): potential and limitations. The Cryosphere, 10, 1075-1088.

Buras, A., A. Rammig, and C. S. Zang. 2019. Quantifying impacts of the drought 2018 on European ecosystems in comparison to 2003. Biogeosciences Discuss. 2019:1-23Cedrá, A. & Lasanta, T. (2005): Long-term erosional responses after fire in the Central Spanish Pyrenees 1. Water and sediment yield. Catena 60, 59-80.

Claverie, M., J. Ju, J. G. Masek, J. L. Dungan, E. F. Vermote, J. C. Roger, S. V. Skakun, and C. Justice. 2018. The Harmonized Landsat and Sentinel-2 surface reflectance data set. Remote Sensing of Environment 219:145-161.

Cohen, W. B., Z. G. Yang, and R. Kennedy. 2010. Detecting trends in forest disturbance and recovery using yearly Landsat time series: 2. TimeSync - Tools for calibration and validation. Remote Sensing of Environment 114:2911-2924.

Colomina, I. & Molina, P. 2014. Unmanned aerial systems for photogrammetry and remote sensing: A review. ISPRS Journal of Photogrammetry and Remote Sensing, 92, 79–97.

D'Oleire-Oltmanns, S., Marzolff, I., Peter, K. & Ries, J. 2012. Unmanned Aerial Vehicle (UAV) for monitoring soil erosion in Morocco. Remote Sensing, 4, 3390-3416.

Dimosthenis C.T., Stamatia, B. & Panagiotis, G.S. 2019. Review on UAV-Based Applications for Precision Agriculture. Information, 10,349, 1-26.

Dostálová, A., Hollaus, M., Milenković, M., Wagner, W., 2016. Forest area derivation from sentinel-1 data. ISPRS Annals of the Photogrammetry, Remote Sensing and Spatial Information Sciences, 3, 227.

Drusch, M., U. Del Bello, S. Carlier, O. Colin, V. Fernandez, F. Gascon, B. Hoersch, C. Isola, P. Laberinti, P. Martimort, A. Meygret, F. Spoto, O. Sy, F. Marchese, and P. Bargellini. 2012. Sentinel-2: ESA's Optical High-Resolution Mission for GMES Operational Services. Remote Sensing of Environment 120:25-36.

Einzmann, K., Immitzer, M., Böck, S., Bauer, O., Schmitt, A., Atzberger, C., 2017. Windthrow Detection in European Forests with Very High-Resolution Optical Data. Forests 8, 21. https://doi.org/10.3390/f8010021

Felderhof, L. & Gillieson, D. 2011. Near-infrared imagery from unmanned aerial systems and satellites can be used to specify fertilizer application rates in tree crops. Canadian Journal of Remote Sensing 37(4), 376–386.

Gao, B. C. 1996. NDWI - A normalized difference water index for remote sensing of vegetation liquid water from space. Remote Sensing of Environment 58:257-266.

Getzin, S., Wiegand, K. & Schöning I. 2012. Assessing biodiversity in forests using very high-resolution images and unmanned aerial vehicles. Methods in Ecology and Evolution 3(2), 397–404.

Ginzler, C., and M. L. Hobi. 2015. Countrywide Stereo-Image Matching for Updating Digital Surface Models in the Framework of the Swiss National Forest Inventory. Remote Sensing 7:4343-4370.

González-Jorge, H., Martínez-Sánchez, J., Bueno, M. & Arias, P. 2017. Unmanned aerial systems for civil applications: a review. Drones, 1, 2, 1-19.

Gorelick, N., M. Hancher, M. Dixon, S. Ilyushchenko, D. Thau, and R. Moore. 2017. Google Earth Engine: Planetary-scale geospatial analysis for everyone. Remote Sensing of Environment 202:18-27.

Grabherr, W. 1936. The dymics of forest fire vegetation on limestone and dolomite soils in the Karwendelgebirge [Die Dynamik der Waldbrandflächenvegetation auf Kalk- und Dolomitböden im Karwendelgebirge]. Beihefte im Botanischen Centralblatt, Band LV, Abteilung B, Heft 1/2.

Gu, Y. X., E. Hunt, B. Wardlow, J. B. Basara, J. F. Brown, and J. P. Verdin. 2008. Evaluation of MODIS NDVI and NDWI for vegetation drought monitoring using Oklahoma Mesonet soil moisture data. Geophysical Research Letters 35.

Guisan, A., and N. E. Zimmermann. 2000. Predictive habitat distribution models in ecology. Ecological Modelling 135:147-186.

Hansen, M. C., P. V. Potapov, R. Moore, M. Hancher, S. A. Turubanova, A. Tyukavina, D. Thau, S. V. Stehman, S. J. Goetz, T. R. Loveland, A. Kommareddy, A. Egorov, L. Chini, C. O. Justice, Townshend, J. R. G., 2013. High-Resolution Global Maps of 21st-Century Forest Cover Change. Science, 850–53. Data available on-line at: http://earthenginepartners.appspot.com/science-2013-global-forest.

Harwin, S., Lucieer, A. & Osborn, J. 2015. The impact of the calibration method on the accuracy of point clouds derived using unmanned aerial vehicle multi-view stereopsis. Remote Sensing, 7 9, 11933-11953.

Hausberger, M. 2016. Sediment removal and morphodynamic processes on the burnt area [Sedimentabtrag und morphodynamisches Prozessgeschehen auf der Brandfläche] Hochmahdkopf (Absam/ Halltal). MSc-Thesis, Leopold- Franzens- University Innsbruck, Institute of Geography.

Hinkley, E. & Zajkowski, T. 2011. USDA forest service-NASA: unmanned aerial systems demonstrations—pushing the leading edge in fire mapping. Geocarto International 26(2), 103–111.

Hirschmugl, M., Gallaun, H., Dees, M., Datta, P., Deutscher, J., Koutsias, N., Schardt, M., 2017. Methods for Mapping Forest Disturbance and Degradation from Optical Earth Observation Data: a Review. Current Forestry Reports, 3, 32-45.

Hormes, A., Adams, M., Amabile, A.S., Blauensteiner, F., Demmler, C., Fey, C., Ostermann, M., Rechberger, C., Sausgruber, T., Vecchiotti, F., 2020. Innovative methods to monitor rock and mountain slope deformation. Geomechanics and Tunnelling, 13(1), 88-102.

Hugenholtz, C.H., Whitehead, K. Brown, O. Barchyn, T.E., Moorman, B.J., LeClair, A. Riddell, K. & T. Hamilton 2013. Geomorphological mapping with a small unmanned aircraft system (sUAS): Feature detection and accuracy assessment of a photogrammetrically-derived digital terrain model. Geomorphology, 194, 16-24.

ICAO 2020. Official website of the International Civil Aviation Organization (http://www.icao.int), last accessed 18.02.2020.

Ionita, M., L. M. Tallaksen, D. G. Kingston, J. H. Stagge, G. Laaha, H. A. J. Van Lanen, P. Scholz, S. M. Chelcea, and K. Haslinger. 2017. The European 2015 drought from a climatological perspective. Hydrology and Earth System Sciences 21:1397-1419.

Kellndorfer, J., 2019. Using SAR Data for Mapping Deforestation and Forest Degradation. In: A.I. Flores-Anderson, K.E. Herndon, R.B. Thapa, E. Cherrington (Eds.), The Synthetic Aperture Radar (SAR) Handbook: Comprehensive Methodologies for Forest Monitoring and Biomass Estimation. National Space Science and Technology Center, Huntsville, pp. 65-172.

Key, C. H., and N. C. Benson. 2006. Landscape Assessment: Ground measure of severity, the Composite Burn Index; and Remote sensing of severity, the Normalized Burn Ratio. Report RMRS-GTR-164-CD: LA 1-51, Ogden, UT.

Koh, L.P. & Wich, S.A. 2012. Dawn of drone ecology: low-cost autonomous aerial vehicles for conservation. Tropical Conservation Science 5:121–132.

Jensen, J. R. 2007. Remote Sensing of the Environment: An Earth Resource Perspective. Pearson Prentice Hall.

Larsen, Y., Marinkovic, P., Dehls, J.F., Bredal, M., Bishop, C., Jøkulsson, G., Gjørvik, L.-P., Frauenfelder, R., Salazar, S.E., Vöge, M., Costantini, M., Minati, F., Trillo, F., Ferretti, A., Capes, R., Bianchi, M., Parizzi, A., Brcici, R., Casu, F., Lanari, R., Manunta, M., Manzo, M., Bonano, M., De Luca, C., Onorato, G., Zinno, I., 2019. European ground Motion Service: Service Implementation Plan and Product Specification Document., Copernicus.

Lechner, V., Adams, M., Schnabel, G. & Schüler, S. 2019a. Classification of mycosis in Pinus nigra stands with UAV-P. Geophysical Research Abstracts, Vol. 21, EGU2019-5751, EGU General Assembly 2019.

Lechner, V., Simon, A., Sotier, B. & Adams, M. 2019b. Monitoring einer Waldbrandfläche mit Methoden der Nahbereichserkundung. Sammelband 'Waldbrände in den Nordtiroler Kalkalpen' (Hrsg. Sass, O.), Innsbrucker Geographische Studien, 41, 209-217.

Lechner, V., Sotier, B. & Adams, M. 2018. Post-event wildfire monitoring with close-range photogrammetry. Geophysical Research Abstracts, 20 (EGU2018-14874), EGU General Assembly 2018 8-13 Apr. 2018, Vienna.

Leistner, I. 2011. Soil erosion dynamics on the Issanger fire area [Bodenabtragsdynamik auf der Issanger-Brandfläche] (Halltal/Karwendel). MSc-Thesis, Leopold- Franzens- University Innsbruck, Institute of Geography.

Liu, C. L., B. F. Wu, Y. C. Tian, W. B. Xu, and J. X. Huang. 2004. Crop drought monitoring using serial NDVI&NDWI in Northern China. Igarss 2004: Ieee International Geoscience and Remote Sensing Symposium Proceedings, Vols 1-7:2264-2267.

Lucieer, A., Turner, D., King, D.H. & Robinson, S.A. 2014. Using an Unmanned Aerial Vehicle (UAV) to capture micro-topography of Antarctic moss beds. International Journal of Applied Earth Observation and Geoinformation, 27, 53-62.

Mayr, A., Rutzinger, M., Bremer, M., Geitner, C. 2016. Mapping eroded areas on mountain grassland with terrestrial photogrammetry and object-based image analysis. ISPRS Annals of the Photogrammetry, Remote Sensing and Spatial Information Sciences, Vol. III-5.

Meyer, F., 2019. Spaceborne Synthetic Aperture Radar: Principles, Data Access, and Basic Processing Techniques. In: A.I. Flores-Anderson, K.E. Herndon, R.B. Thapa, E. Cherrington (Eds.), The Synthetic Aperture Radar (SAR) Handbook: Comprehensive Methodologies for Forest Monitoring and Biomass Estimation. National Space Science and Technology Center, Huntsville, pp. 21-64.

Molina, J.-L., Rodríguez-Gonzálvez, P., Molina, C., González-Aguilera, D. & Espejo, F. 2013. Geomatic methods at the service of water resources modelling. Journal of Hydrology, 509, 150–162

Moser, B., Temperli, C. & Schneiter, G. 2010. Potential shift in tree species composition after interaction of fire and drought in the Central Alps. European Journal of Forest Research 129, 625-633.

Nex, F. & Remondino, F. 2014. UAV for 3D mapping applications: a review. Applied Geomatics, 6, 1-15.

Niethammer, U., James, M.R., Rothmund, S., Travelletti, J. & Joswig, M. 2012. UAV-based remote sensing of the Super-Sauze landslide: evaluation and results. Engineering Geology. 128, 2-11.

Paneque-Galvez, J., McCall, M.K., Napoletano, B.M., Wich, S.A. & Koh, L.P. 2014. Small drones for community-based forest monitoring: an assessment of their feasibility and potential in tropical areas. Forests 5(6): 1481–1507.

Pestalozzi, G. 2019. WSL analyzes the drought of 2018. https://www.wsl.ch/en/news/2019/03/wsl-analyzes-the-drought-of-2018.html.

Psomas, A., Ginzler C., Steinmeier C. 2019. Drought 2018: Analysing the effects on Swiss forest ecosystms using remote sensing. Interner Bericht BAFU/WSL. Nicht veröffentlicht.

Rosnell, T. & Honkavaara, E., 2012. Point cloud generation from aerial image data acquired by a quadrocopter type micro unmanned aerial vehicle and a digital still camera. Sensors, 12, 453–480.

Ruhm, W., Schüler, S., Adams, M., Bauerhansl, C., Hoch, G., Schadauer, K. & Kleemayr, K. 2018. Schwarzkiefer am Limit!? Monitoring von Überleben und Wachstum einer Charakterart in autochthonen und sekundären Waldbeständen unter sich ändernden Umweltbedingungen. BFW-internal project report in German (not published).

Rüetschi, M., Small, D., Waser, L.T., 2019. Rapid detection of windthrows using Sentinel-1 C-band SAR data. Remote Sens. 11, 115. https://doi.org/10.3390/rs11020115

Ryan, J. C., Hubbard, A. L., Box, J. E., Todd, J., Christoffersen, P., Carr, J. R., Holt, T. O. & Snooke, N. 2015. UAV photogrammetry and structure from motion to assess calving dynamics at Store Glacier, a large outlet draining the Greenland ice sheet. The Cryosphere, 9, 1–11.

Sass, O., Hell, M., Leistner, I., Stöger, F., Wetzel, K.-F. & Friedmann, A. 2012. Disturbance, geomorphic processes and regeneration of wildfire slopes in North Tyrol. Earth Surface Processes and Landforms 37, 8, 883-889.

Siqueira, P., 2019. Forest Stand Height Estimation. In: A.I. Flores-Anderson, K.E. Herndon, R.B. Thapa, E. Cherrington (Eds.), The Synthetic Aperture Radar (SAR) Handbook: Comprehensive Methodologies for Forest Monitoring and Biomass Estimation. National Space Science and Technology Center, Huntsville, pp. 173-206.

Shakesby, R. A. & Doerr, S. H. 2006. Wildfire as a hydrological and geomorphological agent. Earth-Science Reviews 74, 269–307.

Shimizu, K., R. Ponce-Hernandez, O. S. Ahmed, T. Ota, Z. C. Win, N. Mizoue, and S. Yoshida. 2017. Using Landsat time series imagery to detect forest disturbance in selectively logged tropical forests in Myanmar. Canadian Journal of Forest Research 47:289-296.

Small, D., Rohner, C., Miranda, N., Rüetschi, M., Schaepman, M.E., 2019. Wide-area Analysis Ready Radar Backscatter Composites. Im Review.

Small, D., 2011. Flattening Gamma: Radiometric terrain correction for SAR imagery. IEEE Trans. Geosci. Remote Sens. 49, 3081–3093. https://doi.org/10.1109/TGRS.2011.2120616

Sortier B., Graf A. & Kleemayr K. 2012. Einsatz von UAV in Forstwirtschaft und Naturgefahrenmanagement. Journal of Torrent, Avalanche, Landslide amd Rock Fall Engineering, 76, 169.

Stubenböck, F. 2016. Effect of forest fire on the mortality and regeneration capacity of protection forest in the inner alpine region using the Absamer Vorberg case study [Effekt von Waldbrand auf die Mortalität und Regenerationsfähigkeit von Schutzwald im inneralpinen Raum am Fallbeispiel Absamer Vorberg]. MSc-Thesis, University of Natural Resources and Applied Life Sciences, Institut of Silviculture.

Tang, L. & Shao, G. 2015. Drone remote sensing for forestry research and practices. Journal of Forest Research, 26, 4, 791–797.

Tonkin, T.N., Midgley, N.G., Graham, D.J. & Labadz, J.C. 2014. The potential of small unmanned aircraft systems and structure-from-motion for topographic surveys: A test of emerging integrated approaches at Cwm Idwal, North Wales. Geomorphology, 226, 35-43.

Tiroler Landesforstdienst (1985): flächenwirtschaftliches Projekt Absamer Vorberg 1985. Landesforstdienst, Tirol.

Tiroler Landesforstdienst 2014. Flächenwirtschaftliches Projekt Absamer Vorberg 2014. Landesforstdienst, Tirol.

Turner, D., Lucieer, A. & Watson, C. 2012. An automated technique for generating georectified mosaics from ultra-high resolution unmanned aerial vehicle (UAV) imagery, based on structure from motion (SfM) point clouds. Remote Sensing, 4, 1392-1410.

Usbeck, T., 2015. Wintersturmschäden im Schweizer Wald von 1865 bis 2014. Schweizerische Zeitschrift für Forstwes. 166, 184–190. https://doi.org/10.3188/szf.2015.0184

Vander Jagt, B., Lucieer, A., Wallace, L., Turner, D. & Durand, M. 2015. Snow depth retrieval with UAS using photogrammetric techniques. Geosciences, 5, 264–285.

Verhoeven, G. 2011. Taking computer vision aloft – archaeological three-dimensional reconstructions from aerial photographs with Photoscan. Archaeological Prospection 18, 67-73.

Wang, Y.Y., Bai, G.X., Shao, G.F. & Cao, Y.K. 2014. An analysis of potential investment returns and their determinants of poplar plantations in state-owned forest enterprises of China. New Forest 45(2), 251–264.

Waser, L. T., C. Fischer, Z. Y. Wang, and C. Ginzler. 2015. Wall-to-Wall Forest Mapping Based on Digital Surface Models from Image-Based Point Clouds and a NFI Forest Definition. Forests 6:4510-4528.

Waser, L. T., C. Ginzler, and N. Rehush. 2017. Wall-to-Wall Tree Type Mapping from Countrywide Airborne Remote Sensing Surveys. Remote Sensing 9.

Watts, A.C., Ambrosia, V.G. & Hinkley, E.A. 2012. Unmanned aircraft systems in remote sensing and scientific research: classification and considerations of use. Remote Sensing 4, 1671-1692.

Weber, D., Rosset, C., 2019. Waldmonitoring mit Sentinel-2 Satellitenbildern. Berner Fachhochschule BFH-HAFL, Zollikofen, Schweiz.

Wiegand, C., Rutzinger, M., Heinrich, K., Geitner, C. 2013. Automated extraction of shallow erosion areas based on multi-temporal ortho-imagery. Remote Sensing, 5, 2292-2307.

Wittenberg, L., Malkinson, D., Beeri, O., Halutzy, A., Tesler, N. 2007. Spatial and temporal patterns of vegetation recovery following sequences of forest fires in a Mediterranean landscape, Mt. Carmel Israel. Catena: 71, 76-83.

Wüest, R. O., A. Bergamini, K. Bollmann, and A. Baltensweiler. 2020. LiDAR data as a proxy for light availability improve distribution modelling of woody species. Forest Ecology and Management 456:117644.